Analyses of Dust Coma Morphology of Comet Hyakutake (1996 B2) Near Perigee: Outburst Behavior, Jet Motion, Source Region Locations, and Nucleus Pole Orientation

David G. Schleicher and Laura M. Woodney

Lowell Observatory
1400 W. Mars Hill Road
Flagstaff, Arizona 86001

Accepted by *Icarus,* 17 October 2002

The Lowell Observatory Preprint Series

Analyses of Dust Coma Morphology of Comet Hyakutake (1996 B2) Near Perigee: Outburst Behavior, Jet Motion, Source Region Locations, and Nucleus Pole Orientation

David G. Schleicher and Laura M. Woodney
Lowell Observatory, 1400 W. Mars Hill Road, Flagstaff, Arizona 86001
phone (928) 774-3358, fax (928) 774-6294
E-mail: dgs@lowell.edu; woodney@lowell.edu

ABSTRACT

We present inner-coma dust imaging of Comet Hyakutake (1996 B2) obtained on 11 consecutive nights in late March 1996, an interval including a major outburst and the comet's closest approach to Earth. The evolution of the outburst morphology is followed, along with the motion along the tail of several outburst fragments. Two spiral dust jets — a primary jet, along with a much weaker secondary jet — are visible throughout the interval and are produced by two source regions on a rotating nucleus. These are examined as a function of rotational phase and viewing geometry, with their appearance changing from a nearly face-on view on March 18 to side-on by March 28. The dust outflow velocity as a function of distance from the nucleus is derived, with the dust continuing to accelerate to a distance of 4000 km or more, and reaching an average outflow velocity of 0.38 km s^{-1} between 3000-8000 km. We present details of our Monte Carlo modeling of the jets and our methodology of fitting the model to the images. The modeling yields the pole orientation of the nucleus, with an obliquity of approximately 108°, corresponding to an RA of 13^h41^m and a Dec of –1.1°. For an assumed spherical nucleus, the primary active region is centered at approximately –66° latitude, has a radius of about 56°, and therefore covers about 22% of the surface. The source of the secondary jet is at a latitude of –28°, has a radius of about 16°, and is located at a longitude nearly 180° away from the primary source. Estimated uncertainties for the pole orientation and the source locations and sizes are each about 3°. This solution for the nucleus orientation and source locations explains the strong asymmetry in measured production rates before and after perihelion in radio observations (Biver *et al.* 1999). The modeling also tightly constrains the sidereal rotation period as 0.2618±0.0001 day, completely consistent with the expected +0.0003 day difference from the observed solar rotation period of 0.2614±0.0004 day determined by Schleicher and Osip (2002), given the pole orientation and position of the comet in its orbit.

Key Words: Hyakutake, comets, coma, jets, rotation

I. INTRODUCTION

In March 1996, the close passage of Earth by Comet Hyakutake (1996 B2) allowed a variety of near-nucleus coma studies to be made. Of these studies, the investigation of time-variable coma morphology was particularly appropriate for several reasons. First, dust jets were detected and seen to move by about 20° in only 30 minutes of time on March 19 by West and Hainaut (1996); their rapid report of this phenomenon alerted other observers to a likely fast rotation period for the nucleus and the need for temporal monitoring. This was confirmed one day later by Jorda *et al.* (1996), who reported at least two jets rotating clockwise and a possible period near 6.6 hr. Jets and shell-like structures were also subsequently reported by Boehnhardt and Barnbandner (1996). Second, Hyakutake was the brightest comet to come close to Earth since the wide-spread use of digital array detectors, permitting high spatial resolution imaging from ground-based observatories, both at visible and IR wavelengths. Third, the orbital characteristics of the comet meant that a rapid change of viewing geometries would occur at and shortly following perigee, essentially allowing observers to obtain the equivalent of a medical CT or MRI scan over only a few days time. The resulting 3-D view would be the first for a comet since the spacecraft flybys of Halley in March 1986; however, these flybys were too rapid to directly measure the motion of dust jets due to nucleus rotation. Finally, several fragments were reported to drift tailwards during the last week of March (Lecacheux *et al.* 1996a; Tozzi *et al.* 1996; Harris *et al.* 1996; Weaver 1996; Lecacheux *et al.* 1996b) and these fragments appeared to be associated with an outburst detected in Hyakutake's lightcurve (Millis *et al.* 1996).

The multi-instrument visible and near-UV observing campaign conducted from Lowell Observatory included conventional narrowband photometry throughout the apparition, imaging during the second half of March, and long-slit spectrophotometry near closest approach to Earth. Our initial analysis (Schleicher *et al.* 1998a) focused on the periodic lightcurve from photometry (Millis *et al.* 1996) and repeating morphological features (Schleicher *et al.* 1996) to derive a rotation period of 6.23±0.03 hr. With the inclusion of additional lightcurve data from Lisse *et al.* (1999), we performed a new analysis of Hyakutake's solar (i.e. synodic) rotation period, yielding the value of 6.274±0.007 hr (0.2614±0.0004 day) (Schleicher and Osip 2002). The combined data sets also allowed us to tightly constrain the onset of the outburst to within a few hours of March 19.9. In addition, the photometry obtained throughout the apparition was used by Schleicher and Osip to examine the heliocentric distance dependencies of the production rates, and determine gas abundance ratios, dust colors, and the effective active area as a function of time.

In this paper, we return our attention to the inner-coma dust morphology exhibited by Hyakutake during the second half of March. While our initial rotational analysis described the periodic release of a primary and a secondary puff or blob of material in the sunward direction (Schleicher *et al.* 1998a), improved image enhancement techniques reveal the underlying jet-like structures seen by some other observers. Our images were obtained on 11 consecutive nights from March 18 to March 28. The dust was isolated by use of a red, narrowband filter on the nights of March 23-25, and a broadband R filter on all other nights. Here we present an overview of the morphology during this interval, including the evolution of the outburst from night to night and our measurements of several outburst fragments moving down the tail. The appearance of the dust jets also varied dramatically near the end of this interval due to the rapid change in viewing geometry. We present details of our Monte Carlo modeling of the jets and our methodology of fitting the model to the images. The dust outflow velocity as a function of distance from the nucleus is derived. We conclude with our best overall solution for the orientation of the rotation axis, the location and approximate size of each of the two active regions, and a discussion of the seasonal consequences of these results.

II. OBSERVATIONS, REDUCTIONS, AND PROCESSING

All eleven nights of dust imaging described here were obtained with the John S. Hall 42-inch (1.1-m) telescope at Lowell Observatory. Two CCD systems were used: a TI 800^2 chip with 2×2 on-chip binning, resulting in a scale of 0.724 arcsec/pixel; and a Thompson 7883 384×586 chip with a 0.519 arcsec/pixel scale. The resulting spatial scale at the comet ranged from 183 km/arcsec on March 18 to 74 km/arcsec at perigee (March 25). The viewing geometry also changed drastically during the 11-day interval, with the phase angle varying by 57° and the position angle of the sun varying by 262°, including a 124° change in just 3.2 hrs on March 27. On March 23-25, narrowband filters from the IHW comet set were used, of which only images obtained with the red continuum (RC) filter centered at 6840Å are presented here. On all eleven nights, images were obtained with a broadband, Kron-Cousins R filter; a comparison of near-simultaneous R and RC images on the 24th confirmed that the locations of the jets in the R images were not affected by gas contamination, and so the jets seen in the R band images on other nights were indeed composed of dust. As displayed in the rotational phase coverage plot in Figure 1, we obtained full rotational sequences on March 23 and 24, and nearly complete cycles on the 25th and 28th; the 25th having a 2 hr gap within a 1.6 cycle session. Approximately half-cycle coverage was obtained on the 20th, 26th, and 27th, with spot coverage on the remaining nights of the 18th, 19th, 21st, and 22nd. A summary of the observational parameters, such as the heliocentric distance (r_H), geocentric distance (Δ), phase angle, and position angle of the sun, at the mid-time for each night is given in Table I, including a range of values within individual nights when a particular parameter was changing rapidly.

Typical exposure times ranged from 1 to 15 seconds with the R filter, and 10 to 30 seconds for the RC filter. IHW flux standards were measured on the 23rd, 24th, and early on the 25th (before conditions became non-photometric); except for the 19th, the other nights were non-photometric. Nightly mean bias and flat frames were determined and applied to the comet images. In the case of the Thompson CCD, which is thermoelectrically cooled, dark frames were also determined and removed. On some nights, multiple R frames were obtained within an interval of less than 10 minutes; in these cases, we computed a single median image to improve the S/N. All images were normalized for exposure time and extinction corrected for airmass, and the photometric RC observations were flux calibrated. However, in the analysis of the dust morphology, flux calibration was not necessary — relative brightnesses of morphological features within images are modeled, rather than brightness variations between images — and, as already noted, was not possible for most nights. Therefore, the normalization procedure described next, which we applied to non-photometric images, was primarily intended simply to minimize artificial brightness variations due to changing cloud conditions.

After shifting the comet to the center of each frame as detailed later, non-photometric images were normalized to keep the total brightness constant during a night within a 50×50 arcsec box centered on the comet; this size box was chosen to minimize brightness variations due to rotational phase. Each night's images were then renormalized to the 19th using a method to remove the effects of the outburst on the fluxes when making night-to-night comparisons, by forcing the flux in a sunward hemispheric annulus to be constant. This region was defined by 180° centered on the position angle of the sun, with an inner radius of 660 km and an outer radius of 6600 km projected distance. As we show in Section III, this effectively excludes the tail and nearly all material released in the outburst. However, this technique yielded a trend over time due to the changing viewing geometry, which we will also address in Section III. Because sky values could not be extracted from the frames due to the comet overfilling the image, sky values were based on typical values from photometric nights (with and without the moon up). An iterative procedure was developed to adjust the normalization scaling factor and sky values until the coma value within the hemispheric annulus reached the desired value. Specifically, the sky was subtracted and a scaler was applied iteratively until the hemispheric annulus value and a location near the edge of the frame matched the reference image. This procedure confirmed that the sky values were very low and any errors introduced were negligible. Moreover, the image enhancement techniques (described next) removed any systematics introduced by the normalization technique.

A necessary step prior to our image processing and enhancements was to determine the nominal nucleus location in each frame and shift the image accordingly to center the comet in the frame. The primary centroiding procedure will be discussed in detail in a paper on Comet Hale-Bopp (Farnham *et al.* 2002). Briefly, the approximate location of the nucleus condensation is selected interactively, and a 2-D parabola is fit to determine the initial solution. Then a grid series of $1/\rho$ patterns, convolved with a Gaussian having a FWHM of the typical seeing, is compared to the image, each shifted by a pre-selected interval (typically one-quarter of a pixel), with χ^2 computed for each to determine an improved solution. After applying this procedure to each frame, all resulting images on a given night were used to create a median image. Next, this median image was used instead of the $1/\rho$ pattern, and the process of computing χ^2 at each grid point was repeated. Based on these new χ^2 values, each frame was again shifted. This method greatly minimized small errors in the centroiding introduced by changing jet positions during the night and from night to night; moreover, our preferred image enhancement techniques are relatively insensitive to any errors in the centroiding, which were usually less than 0.3 pixel.

In order to improve the contrast of the jets with respect to the background coma, we experimented with several image enhancement techniques before selecting the methods used here (see also Farnham *et al.* 2002). Our primary requirement was that the bulk radial fall-off be removed without significantly changing the position of the jets. The method we applied to all nights of data was azimuthal median division. To create the azimuthal median we first made a median image for the night. On nights with sufficient rotational coverage, this median was made from a complete rotational sequence (i.e., 6.27 hr) of images and the jets were effectively removed, while on nights with partial rotational coverage we simply medianed together all the images from the night, usually resulting in residual jet features still being visible in the final median image. An azimuthal median radial profile was created from our median image for each night, and this was used to create an azimuthally symmetric synthetic image which was then divided from each individual frame. (While similar to the common method of removing a canonical $1/\rho$ profile, the azimuthal median processing also removes any remaining radial trends in the dust, and also works well with gas species whose radial profiles differ greatly from $1/\rho$.) Due to the relatively benign nature of this enhancement technique, bulk brightness asymmetries and variations in brightness along jets and between jets can be compared to a synthetic, model coma. However, because the tail is often quite prominent and sunward/tailward asymmetries are large in Hyakutake, it can be difficult to track the position of jets into the anti-sunward portion of the frames.

To further improve the visibility of the jets for those nights having near-complete rotational coverage, our second enhancement method effectively removed both bulk azimuthal asymmetries as well as the bright tail following the outburst. In these cases, March 23-25 and 28, the original nightly median images described above contain no residual jets. We were, therefore, able to simply divide each original image by the median image for the appropriate night. This median image division method effectively removed coma structures which were mostly unchanging throughout a night, yielding a resulting image dominated by the rotating jets.

Our final method of image enhancement was developed to bring out the fragments observed moving down the tail following the outburst. The first step was to create a median radial profile from a 90° wedge centered on the tail for each image. Synthetic images were created from these profiles and then the original images were divided by the synthetic ones to remove the bulk tail structure; however, only the brightest of the tail fragments were easily visible after this enhancement. To further enhance the condensations in the tail we used a second order high-pass Butterworth filter (e.g. Gonzalez and Woods 1992). The Butterworth filter is applied in frequency space and allowed us to remove all the low frequency spatial components of the image — leaving us only with features that vary on short spatial scales such as the tail fragments. We applied a frequency cutoff of between 25 and 30 to our images, as this provided the best contrast of the fragments to the surrounding coma. The resulting images clearly show several individual fragments.

Additional processing of each frame involved trimming to a common size (401×401 pixels) and, for final figures, trimming and rebinning to a projected physical size of either 16×10^3 or 20×10^3 km on a side. Stretches and color tables were chosen in an attempt to maintain a consistent brightness and contrast for the primary jet from night-to-night; however, the two different image enhancement techniques required significantly different stretches. A representative example of the results using these techniques is given in Figure 2, where we display an unenhanced dust image from the 25th, our three preferred enhanced versions, along with a version with $1/\rho$ removed and an unsharp masked version. Note that, when working interactively with each image on the computer monitor to follow complete spirals, the image was stretched on-the-fly to maximize contrast in different locations on the frame.

III. Non-Rotational Coma Morphology

The overall coma morphology, and how the appearance of the comet changed with viewing geometry and with the occurrence of the large outburst is demonstrated in Figure 3. Here we show a single representative image from each night, using the azimuthal median image enhancement. The dust tail is readily visible in each frame; at these small spatial scales, the tail is essentially directly anti-sunward. Note the extremely rapid change in geometries on March 26-27 as the comet passed within 4° of the north celestial pole.

As previously indicated, the initiation of the outburst was within a few hours of March 19.9, based on lightcurve measurements (Schleicher and Osip 2002). However, despite the rapid increase in dust production measured on March 20, the comet's appearance on the 20th differs little from that seen on the previous two nights. By the 21st, the outburst is clearly visible, but is still much less apparent than on the 22nd or 23rd, even though the peak in dust production is believed by Schleicher and Osip to have occurred late on the 20th. The cause of this apparent discrepancy is due to the enhancement method. During the initial phase of the outburst, the excess dust is nearly symmetric around the nucleus, and so is removed when the median azimuthal profile is removed. This is confirmed by the >2× excess of flux on March 20 and 21 at $\rho < 1000$ km in the azimuthal median radial profiles (Figure 4). As time progresses, the material is pushed tailward, primarily by radiation pressure for the smallest particles, and by preferential outgassing on the sunward side of larger grains or fragments. Small grains probably continue to be released by the slow-moving larger fragments, explaining the relatively low bulk velocity of the material. By the 22nd and 23rd, essentially all outburst material has moved tailward, yielding the very bright feature in our enhancements. As the dust continues to accelerate and disperse, the large feature nearly disappears, except for a few condensations which can be detected along the tail on March 25-28. From these images it can be seen that the sunward hemispheric annulus defined in Section II for normalization purposes successfully excludes material from the outburst. (As the comet approaches the Earth and goes from a nearly face-on to a side-on appearance over this interval, the normalized azimuthal median radial profile systematically decreases due to our adopted normalization method. As our goal for normalization was to be able to inter-compare the images rather than to attempt absolute flux calibration, this effect is unimportant, but should not be interpreted as an actual fading of the comet.) While the condensations along the tail are clearly associated with fragments, the fragments themselves are much too small to be seen, but rather act as mini-nuclei, each with its own mini-coma. These are best seen with the Butterworth filter image enhancement technique previously described, and a representative image from each night is shown in Figure 5.

A number of these fragments have been measured and modelled previously by Desvoivres *et al.* (1999) and by Desvoivres *et al.* (2000), who deduced release times for the fragments, along with values of ρr, the product of the fragment density and size directly associated with the observed acceleration. Unfortunately, poor weather resulted in a gap of approximately 40 hrs, since no observations were obtained by Desvoivres *et al.* on the night of March 26/27, increasing the possibility of misidentification of individual fragments across this gap. Because of the western location of Lowell Observatory as compared to theirs, fragments were detected on two nights within the gap, making fragment identification less ambiguous. We, therefore, extracted the positions of the fragments we detected on March 25-28, to directly compare to the Desvoivres *et al.* (2000) results. Similar to both Desvoivres *et al.* analyses, we measured the positions of each condensation with respect to the nucleus, confirming that they were directly along the anti-sunward direction as seen on the sky. This fact permitted us to assume they were directly anti-sunward in three-dimensions, thereby allowing us to correct for the projection effect due to the comet's phase angle, yielding a true spatial distance, r, from the nucleus. (This r is distinct from that used in the quantity ρr by Desvoivres *et al.* for the fragment size, as is our quantity ρ, the projected distance, from their fragment density.) These distances, as a function of time, are plotted in Figure 6.

A simple examination of the measurements from night-to-night and the slopes within the nights of the 25th and 28th implies that a minimum of 6 fragments are needed to explain our measurements. It is reasonable to expect that, to first order, a fragment will move down the tail with constant acceleration with respect to the nucleus. Therefore, we have fit the data with curves assuming constant acceleration, for each fragment, and derived both the non-gravitational acceleration, a, and the time of release from the nucleus region, T_0, (see

Figure 6 and Table II). To assist in some of the identifications, we overlaid data from Desvoivres *et al.* (2000) prior to the curve fitting. We label the six identified fragments "A-F", in decreasing order of their distance from the nucleus on March 25th.

Indeed, a direct comparison of our distance vs. time measurements and those plotted in Figure 4 from Desvoivres *et al.* (2000) shows excellent agreement. For instance, our measurements of fragments "B" and "D" on the 26th are at slightly larger distances than Desvoivres *et al.*'s fragments "2" and "5" taken several hours earlier, just as would be expected. On the 28th, our observations of fragment "B" overlap in time and extend past those by Desvoivres *et al.*, and the coincident measurements are essentially an exact match of their fragment "2". We consider the identifications of fragments "B" and "D" as definitive, with both our positional measurements and fitted curves in excellent agreement with those fragments identified by Desvoivres *et al.* (2000) as "2" and "5", respectively. Our fragment "F" is also well-determined and matches their fragment "6" except on March 27/28, where they identify it as "4". We believe that "4" and "6" should be reversed on this night, resulting in a significantly faster acceleration for "4". Fragment "A" is difficult to detect, but when combined with their measurement of "1" on previous nights, we obtain a nearly identical fit to their's based on a shorter time interval. Fragment "C" is also relatively faint, and has no obvious counterpart in the Desvoivres *et al.* measurements, but yields a self-consistent fit. Fragment "E", however, is only clearly detected on March 25; it may overlap fragment "D" ("5") on the 26th, but we have not attempted to fit a curve to "E". Finally, a few other possible detections are shown, but are sufficiently indefinite that we have not labeled them.

We were somewhat surprised at how well the motion of some fragments were fit with the assumption of constant acceleration, as this implies that the rate of outgassing and the mass of the fragment were essentially unchanged. This is consistent with the calculation by Desvoivres *et al.* showing that the expected mass loss of each fragment due to vaporization should be about 1% of the total mass of the fragment during the interval of their measurements. In contrast, it is clear from both data sets that from March 28 through early April fragment "D" ("5") is accelerating somewhat faster than on earlier dates, possibly due to an additional splitting. Brightnesses of several of the mini-comae also vary day-to-day in an irregular manner, also possibly due to subsequent partial fragmentations which expose fresh ice.

While Desvoivres *et al.* (2000) created a sophisticated model for fragment motion — first computing the quantity ρr, and then relating this to the acceleration (a) — we instead utilize their results to compute ρr from our derived values for a. They note that ρr is inversely proportional to a and, based on their modeling, a value of ρr of 5000 kg m^{-2} corresponds to a range of a of $1\text{-}2\times10^{-5}$ m s^{-2}. Adopting the mid-point value of 1.5×10^{-5} m s^{-2}, we compute approximate values for ρr and these are listed in Table II. Our results are within 10% of Desvoivres *et al.* for fragments "A" ("1") and "B" ("2") and within 20% for "D" ("5") and "F" ("6"). If one further assumes a density of 0.5 gm cm^{-3}, these correspond to sizes ranging from about 7-21 m for the smaller fragments and ~50 m for "F".

In addition to the coefficients of the curves listed in Table II, we also provide estimated uncertainties in the value of the non-gravitational acceleration. Because the value of the separation date is strongly dependent on the acceleration, we further list a range of dates due to the uncertainties in a. We note that, given these ranges, it is likely that fragment "C" was released with the initiation of the outburst (approximately March 19.9; see Schleicher and Osip 2002) and that it is plausible that the slow moving fragment "F" was also released at this time. While the data are inconclusive, we suspect that the fragments having release dates subsequent to the initial outburst were calved off of the largest fragment ("7") detected by Desvoivres *et al.* (2000), rather than released directly from the nucleus. This largest fragment's motion was much slower than that of any of the other fragments, and so it only was detected after March 30 when it had drifted sufficiently far down the tail to be distinct from the nucleus. While Desvoivres *et al.*'s modeling of its motion implied that it was released on March 21, given the uncertainty in the extrapolation to a release date, we postulate that this largest fragment broke off the nucleus at the onset of the outburst, i.e., approximately March 19.9. The associated exposure of fresh volatiles to solar radiation produced the rapid release of gas and dust, providing the onset of the outburst detected in the lightcurve. The dust rapidly moved tailward and dispersed, while this largest fragment continued to calve smaller fragments, which subsequently accelerated down the tail and were measured by Desvoivres *et al.* and ourselves. The bulk of the freshly exposed ice on the fragments and the icy grains released near the beginning of the outburst was exhausted within a few days, consistent with the total production rates returning to baseline levels by about March 25, even though the largest fragment was still well within the photometer apertures used by Schleicher *et al.* (1998a) and Schleicher and Osip (2002).

It has long been known that some comet nuclei split into multiple pieces or partially fragment. The most recent example is Comet LINEAR (1999 S4), which first experienced a series of outbursts of varying sizes as it approached the sun, and then completely disintegrated in late July within a few days of perihelion (cf. Kidger 2000; Tozzi and Licandro 2001; Boenhardt 2001). In particular, a fragment was detected moving down the tail of LINEAR in HST images obtained in the days following a large outburst on July 5 (Weaver *et al.* 2001), very similar in nature but on a larger scale with the fragments observed in Hyakutake. It now appears that partial fragmentation of comet nuclei may be a common occurrence, but is seldom directly detected because of insufficient spatial resolution and/or insufficient temporal coverage.

IV. ROTATIONAL COMA MORPHOLOGY AND MEASUREMENTS

The general appearance of the inner-most coma of Comet Hyakutake only began to change rapidly on March 26, as is evident in the sequence of images presented in Figure 3 and the viewing geometry parameters given in Table I. In particular, until the 26th, the primary jet essentially appears face-on. This is most readily seen using the median rotational sequence image enhancement method, where the bulk asymmetries and the tail are nearly completely removed. A representative rotational sequence from March 24 is shown in Figure 7, where the interval between frames is approximately 94 minutes (0.25 phase). A GIF animation of a similar sequence, but having additional intermediate frames, is available on the web [www.lowell.edu], along with a sequence showing the corresponding CN gas jets. These animation loops — particularly that of CN — unambiguously show complete spirals and that we, on Earth, appear to be looking from within the cone swept out by the jet as the comet rotated. However, by the night of March 28, it is evident from a similar rotational sequence shown in Figure 7 that we are now seeing the spirals approximately side-on, with all jet structures contained within the sunward hemisphere on the plane of the sky, and with jets overlapping due to projection effects.

An examination of these sequences, along with all of the other dust images during this 11-day interval, allows us to arrive at some basic conclusions. First, we can confirm the preliminary results from Schleicher *et al.* (1998a) that a single, primary jet dominated the morphology and caused the periodic rotational lightcurve that was observed. Second, a much weaker jet, not detected in the lightcurve, is offset by about one-half cycle from the primary jet. We can further conclude that the active region which is the source of the primary jet is probably quite large in relation to the size of the nucleus, because the jets appear much broader and more diffuse than in Comets Hale-Bopp or Halley; in fact, Schleicher *et al.* (1998a) called them puffs or blobs for this reason. Finally, the presence of complete spirals seen from varying viewing angles provided an excellent opportunity to uniquely determine the orientation of Hyakutake's rotation axis in space and the location of the active regions.

In order to both extract dust outflow velocities and quantitatively compare the jet morphology with Monte Carlo jet modeling, our first step was to measure the location of the jets as a function of time. Our methodology is the same as what we have used in our ongoing Hale-Bopp analyses (Schleicher *et al.* 1998; Farnham *et al.* 1999), and we again defer a detailed discussion to the paper by Farnham *et al.* (2002). In brief, we extract 36 radial profiles from each enhanced image, where each profile is the mean from a collapsed 10° wedge, thereby compensating for the decreasing signal as a function of projected distance from the nucleus. The relatively broad peaks within each radial profile are then interactively fit with a parabola, and the locations of the fitted peaks are recorded, and then converted from pixels to projected distances in kilometers of the brightest location in each jet at each of the 36 position angles.

The associated uncertainty for an individual measurement depends on the intensity and width of the jet, along with any trends with distance in the residual background. Because these characteristics change with distance, position angle, and image enhancement technique, the associated uncertainty can vary from between one and several pixels. Also, small systematic offsets were evident among the different image enhancement techniques, due to differing residual background slopes. An examination of this phenomenon confirmed that our median image division technique best removed background slopes, while the azimuthal median division often yielded measured positions of the dust jets smaller by 2-3 pixels. Fortunately, there was no trend with distance in these offsets due to enhancement techniques, so derived velocities are unaffected.

The resulting radial distances of the jet as a function of time for a given position angle (PA) can be plotted and, because of our good temporal coverage within several of the nights, positions associated with an individual jet can be identified. A composite plot showing the jets' radial motion on the 24th is given in the top panel of Figure 8 for all PAs having well-identified jet features. Both jets are evident in this representation, with the primary jet extending out past 10^4 km, while the secondary jet (to the left) was too faint and diffuse to be detected in any direction beyond about 5000 km. To obtain this composite plot, we combined measurements of 3 successive rotational cycles on the 24th, even though observations were only obtained during 4/3rds of a rotational cycle. This was possible because two rotational cycles of the primary jet are usually visible in each individual image, with the positions of the outer spiral corresponding to material released one cycle earlier than the inner spiral. Since the jet's appearance was nearly identically after one cycle, the outer spiral measurements could be used to effectively extend the temporal coverage by transposing the times by one period (6.27 hr), as if they were obtained one cycle later. This procedure allowed us to utilize all measurements of each jet on a single night and to track the motion of a jet to greater distances than otherwise possible.

Most of the apparent scatter in this composite plot (Figure 8, top) is due to differing projection effects as a function of PA. To distinguish this variation with PA, we have assigned different symbols in successive groups of 60° (see key). In principle, we could use the measured distances as a function of time at any single PA in order to determine the projected dust velocity, and then remove the projection effect with the subsequent Monte Carlo modeling. However, by combining measurements at many PAs, we can obtain a more robust solution, and we have done so using the method described next.

At each PA for which one or both jets can be well-identified, the jets' radial motion clearly accelerates out to projected distances of about 2000-3000 km. Between about 3000 and 8000 km, the curvature in the jets' radial motion is much less but often still discernable. In those cases for which the primary jet is detected beyond 8000 km, a *decrease* in the velocity becomes evident, presumably due to radiation pressure (note that the jet is only detected beyond 8000 km for PAs in the general sunward direction). The curvature between 3000 and 8000 km is sufficiently small that the data in this regime can be approximately fit with a linear function to derive an average projected velocity at each PA. These linear least-squares fits can then be used to determine and apply a first-order correction for the relative projection effects at different PAs.

The extracted projected average velocities for the primary jet are plotted in Figure 9 as a function of PA for PAs ranging from 280° (–80°) to 150°; there are insufficient data beyond 3000 km to determine velocities for the primary jet at other PAs, and for the secondary jet at all PAs. We further distinguish between PAs at which the jet's radial motion is well-defined out to 8000 km (filled symbols) and those which are incomplete or show distortions (open symbols). Because it is the same jet measured at each position angle, differences in slopes must be caused by relative projection effects, and the PAs exhibiting the largest well-determined average velocities must have the smallest projection effects. Limiting this examination to points having relatively small uncertainties in their fits (<0.02 km s^{-1}), it is apparent from Figure 9 that the maximum projected average velocity between 3000 and 8000 km is about 0.38 km s^{-1}. If we assume that velocities less than this value at other PAs are simply due to changing projection effects, we can adjust the projected distances based on the ratio of extracted velocities to correct for differing projection effects as a function of PA. For instance, the projected distances at PA=30° were scaled by the factor 0.38/0.333. The result is shown in the middle panel of Figure 8, where the radial motion data of the primary jet at each PA having a well-defined curve (those having filled symbols in Figure 9) has been adjusted to the minimum projection corresponding to 0.38 km s^{-1}. (Note that if the jet at any PA is actually in the plane of the sky, then this maximum projected velocity is simply the true radial outflow velocity. As discussed in a later section, our Monte Carlo modeling shows that because of the very broad width of the primary jet, the 0.38 km s^{-1} average projected velocity between 3000 and 8000 km is essentially identical to the true outflow velocity.)

Having adjusted the projected distances, most of the remaining scatter between various PAs (middle panel of Figure 8) is the result of offsets in time, due to projection effects and viewing geometry. We can therefore adjust each of these as well, shifting each curve in time to force fitted portions of each PA curve to match, and therefore obtain a single, overall curve representing the jet's radial motion from its origin at the nucleus. This result is given in the bottom panel of Figure 8. It is clearly evident from this composite curve that the dust associated with the center of the jet continues to accelerate out to at least 4000 km, and possibly out to 8000 km. We computed a simple 2nd-order polynomial fit to the curve inside 8000 km and this fit is overlaid onto the data. This fit, $0.031181*T+6.69682\times10^{-6}*T^2$, where T is the age of the grain since its release from the nucleus, is clearly a good representation of the dust behavior out to at least 4000 km and possibly to 8000 km, before radiation pressure effects dominate.

V. COMET JET AND COMA MODEL

The Monte Carlo (MC) model we have developed was created specifically for the purpose of reproducing jet morphologies in cometary comae. As such, it has several typical features of MC coma modeling routines, some specialized features to assist in searching large parameter spaces, and some simplifications to speed the computations. All calculations are performed in the reference frame of the nucleus, with the comet's orbital plane and the position of the sun at perihelion defining the fundamental cartesian coordinate system. Following the right-hand rule, the orientation of the rotation axis is defined by its tilt with respect to the perpendicular to the orbital plane (i.e., the obliquity) from 0 to 180°, and the direction of the tilt around the orbit (i.e., the orbital longitude of the pole) from 0 to 360°, where zero is defined as anti-sunward at perihelion. A series of coordinate transformations are performed to yield a view in the sky plane as seen from Earth, with north at the top, or in polar coordinates of PA vs ρ directly corresponding to the jet measurements from the previous section. The software package, DataDesk, within which we create the Monte Carlo model, readily permits us to view the model from any of the coordinate systems, as appropriate. We can also interactively vary the value of a parameter and see the resulting effect on-the-fly, thereby permitting a decision of "better or worse" with each change in value.

Having been designed for dust analysis, the model used in the analyses reported here assumes an initial radial outflow of particles from a spherical nucleus, modified by the effects of radiation pressure. Initial outflow velocities and the acceleration of grains as a function of distance from the nucleus are adjustable parameters; for Hyakutake, we assume the functional form of outflow distance with particle age determined in the previous section, with an additional free parameter for scaling this function due to any remaining projection effect not accounted for in the procedure used in Section IV. To mimic the effects of a distribution of particle sizes, a small Gaussian distribution in the effective outflow velocities (a FWHM of ~10% of the functional value) is randomly applied to test particles. The sidereal rotation period is also a free parameter, but is essentially treated as a constant for Hyakutake, where we initially assumed the observed solar period of 0.2614 day (6.274 hr) from Schleicher and Osip (2002). The current model assumes a spherical nucleus and allows up to 3 active areas to be defined as source regions, along with an isotropic, whole-surface component. Each active region is assumed to be circular, with its radius and position (effective latitude and longitude) free parameters. The relative fraction of particles emitted by each region and by the isotropic component can also be varied; here, we initially assumed that 80% of the particles reside in the primary source region, 10% in the secondary source, and 10% were uniformly distributed across the entire surface. (No particles were assigned to the 3rd possible active area in the model, because only 2 jets were detected in the face-on images of Hyakutake.) The amount of dispersion from the local normal direction from the surface can be set, and a 5° Gaussian dispersion was used for most of the simulations. Note that for practical purposes given the scale of the coma compared to the small size of the nucleus, all particles effectively have an initial radial outflow from the origin until radiation pressure modifies their motion, even when released at an angle different than the normal to the surface. Consequently, two sets of surface coordinates were associated with each particle in the computations — a nominal latitude and longitude, for use in computing solar illumination, and an effective latitude and longitude matching a normal surface when applying the directional dispersion.

The total number of particles in the simulation can be altered, but is usually held constant for a specific comet; for Hyakutake, 10^5 particles were used. The desired start date and the observation date are also free parameters, as is the time interval over which the particles are assigned at a uniform rate. Based on the desired proportion between source regions, and assuming uniform probability within the source region, the specific latitude and longitude of origin of each particle on the assumed spherical nucleus is computed randomly, as is the velocity and direction based on the values of the dispersions. The probability that an individual particle is actually released from the surface depends on the position of the sun at the nominal time of release. While this function can be readily changed, we begin by assuming it is simply the cosine of the sun angle, i.e. the cosine of the zenith distance of the sun or the concentration of solar radiation on a normal surface. A small fraction of the particles are also emitted if the sun is below the horizon, primarily to act as tracers of the location of a jet should the source region of the actual comet's jet experience a significant thermal lag. Once the nucleus parameters are tightly constrained by fitting the shapes of the jets, one can adjust this solar illumination function to quantitatively reproduce both the jets' and overall coma intensities.

The primary differences in the current model from the original version used in preliminary modeling of Hale-Bopp (eg., Schleicher *et al.* 1998b; Farnham *et al.* 1999), is a much larger total number of particles and the inclusion of active regions of finite size. The original version was based on the belief that the brightest location within a jet corresponded to the center of the jet, and so only enough particles were included in the simulation to act as tracers of the jet, and these were then compared to the measurements of the jets' position. The advantage of this method was the very fast computation times, with the entire run and re-display taking only a few seconds, thereby allowing us to perform a relatively rapid complete grid-pattern search of our multi-dimensional parameter space. However, the Hale-Bopp analyses (Schleicher *et al.*; Farnham *et al.*) implied that a large precession was required to reproduce the nearly face-on appearance of the Hale-Bopp jets over a 2-month interval, during which the viewing orientation changed by more than 90°. Moreover, the Earth apparently remained preferentially near Hale-Bopp's projected rotation axis throughout the interval, making this solution highly suspect. Subsequently, in an attempt to explain this lack of change in foreshortening of the spiral jets during a large change in viewing geometries without invoking an unlikely precession scenario, Samarasinha (2000) explored the effects of wide jets vs narrow jets on the appearance of spiral patterns. He successfully showed that a wide jet — either due to dispersion from the normal when released or due to a large active region over which the normal direction changes significantly — will produce a much less foreshortened spiral pattern than that produced by a narrow jet. However, complications in the Hale-Bopp morphology, including numerous overlapping jets, prevented Samarasinha from attempting to create a detailed Hale-Bopp model.

Based on Samarasinha's investigations, we added the ability to vary the size of each active region to our model, and increased the number of particles so that densities along and across jets can be determined. An example of the significance of this wide-jet projection effect is shown in Figure 10, where the spiral jet's foreshortening changes dramatically as the source size is altered. Note that the appearance also changes because the duration and intensity of sunlight varies as a function of latitude across the source region. As discussed further in the next section, we can also remove a radial profile, such as $1/\rho$, to more closely mimic our image enhancement techniques when making direct comparisons to the observations. The actual "enhancement" is accomplished by randomly removing particles with a probability function consistent with the desired profile.

VI. THE MODEL FITTING PROCESS

The model fitting process begins by importing the entire set of jet measurements (i.e., the extracted positions of peak intensity; see Section IV) into DataDesk. These measurements are used to interactively create schematic x vs y plots (i.e. as seen on the sky) and PA vs ρ polar coordinate plots for any image or set of images. By stepping through these plots as a function of time or rotational phase, we can follow the outward motion of the jets with time and, when the morphology is relatively simple, uniquely match the measured positions with a specific jet. Animation sequences of the enhanced images are also created in order to resolve any ambiguities regarding the identification of individual jets as they move outward with rotation. These identifications can be attached to the measurements, and color-coded to distinguish the primary and secondary jet throughout the observations. Ultimately, our goal was to use the MC jet model to both reproduce the quantitative measurements of the peak brightness of jets through the coma with time, and the relative intensities throughout the inner coma.
To accomplish this, we used the schematic plots of the measurements as an overlay to each synthetic model image as we searched the entire parameter space (a process described in later paragraphs); a "by eye" comparison to the overlaid positions was readily accomplished because the location of the peak brightness along the model jets was easily discernable. Once the parameter space was reduced to a manageable size, we made use of the enhanced images in our comparisons in addition to the measurements, in order to approximately reproduce the jet width and overall coma asymmetries. While a χ^2 test would have been preferred for this stage, this was impractical for several reasons, including the limited number of particles in the model and the lack of a strong constraint on the particle size distribution or the possible existence of an ambient coma. Instead, we again employed the "by eye" technique, this time changing the value of a model parameter and deciding if the resulting model image was "better or worse" than the previous model image. In practice, we also found that the x vs y plots were most useful in narrowing the parameter space to a small, viable region, but that fine-tuning the parameters to get the best possible fit was best accomplished using the PA vs ρ polar coordinate plots. When available, images enhanced with the median image division technique were used to follow the jet's position in the anti-sunward hemisphere, but all comparisons of relative brightnesses were made using the azimuthal median processing, which most closely matches the $1/\rho$ processing used within the MC model. (Creating stacked median images from the model is impractical when performing searches of a large parameter space. Instead, by testing representative images we have confirmed that measured jet locations typically change by less than 2-3 pixels between removing a $1/\rho$ profile, the azimuthal median profile, or the stacked median image.)

Because of the large number of adjustable parameters in the model, a specific, systematic procedure was developed to ensure that no viable solution is missed during the model fitting. We began by attempting to match the gross morphology of the primary jet in a few frames from March 18, 20, and 24 with a single, narrow jet, performing a (tedious) full grid pattern search of three parameters — pole tilt, pole orbital longitude, and source latitude — which most control the overall appearance of the spiral jet. The tilt and latitude were stepped at 15° intervals while the pole orbital longitude was varied in 30° steps, resulting in 2028 combinations, some of which were redundant (when the tilt is either 0 or 180°). (Note that while we had assigned reasonable values to other parameters such as outflow velocity and radiation pressure, based on the results from the previous section, these did not yet need to be systematically varied because they have little effect on the overall shape of the spiral.) Because Hyakutake's primary jet is clearly a clockwise rotating face-on spiral prior to March 26 (see Figure 3), the majority of these 2028 combinations are easily eliminated, as they produce either counter-clockwise spirals or side-on views. The remaining region was explored with progressively smaller grid spacing to derive a viable region. At this stage, the location along a jet where the jet clearly brightens because the active region has rotated into sunlight is a particularly strong discriminator between combinations of pole tilt and source latitude which otherwise produce very similarly shaped spirals. Sunrise *must* have occurred for the source region prior to the brightening. In contrast, the location along the jet where the brightness decreases is less constraining, because it is *a priori* unknown how long significant activity will continue past sunset due to thermal lags. This process resulted in a viable region of solutions restricted to a pole tilt of between about 140 and 170°, a primary source latitude of about –40 to –20°, and a pole orbital longitude of about 220 to 280°; however, *no* single narrow-jet solution provided a reasonable match to the data throughout the interval.

The entire search process was then repeated for a wide jet, in the case of Hyakutake assuming a source radius of 50°. This both allowed us to understand the specific projection effects previously discussed regarding jet width and to obtain a wide-jet solution set. In this case, our resulting viable region included a pole tilt of about 100 to 120°, a source latitude of –60 to –80°, and a pole orbital longitude of 210 to 250°. We then explored both the narrow and wide jet solution regions, as well as all intermediate parameter combinations, with measurements from additional images at different rotational phases and viewing geometries. (We previously confirmed Samarasinha's (2000) conclusion that the length of the major axis of a foreshortened spiral is largely unchanged as the jet's width is varied; instead, the spiral appears less and less fore-shortened as the jet width is increased due to a progressive lengthening of the minor axis. This fact greatly helped to restrict the parameter space that needed to be searched as the jets were widened.) During this stage of the process, we began adjusting other parameters such as the outflow velocity scaler and source longitude to best reproduce the specific position of the observed jets as a function of rotational phase for each image, rather than just matching gross shape characteristics.

Fortunately, the apparent ambiguity from a change in jet width mimicing a change in pole orientation can be resolved by several means. First, an incorrect solution will yield a changing pole orientation that follows the observer as the viewing geometry changes. Second, an incorrect solution can also result in an apparent change in outflow velocities due to changing geometries. Both of these artifacts should be eliminated by correctly-sized source regions. Third, increasing the source/jet width produces features, such as material moving outward along the rotation axis, which either do or do not exist in the images. The presence of these extra features, and the need to avoid generating non-existent features, provides an additional strong constraint on the size and location of the source regions. In fact, some unexplained features seen in the images, such as a near-circular feature in the innermost coma, were created naturally as the primary jet's radius increased beyond about 30°.

Once a nominal solution, along with a surrounding region of parameter space of viable solutions was determined, the parameter search process was repeated for the secondary jet, only skipping the initial, course-grid stage. In the case of Hyakutake, this yielded a similar but less-well constrained region of parameter space with that we obtained for the primary jet. Finally, both jets were included simultaneously in the model, and we iteratively fine-tuned parameters to yield a best combined solution for images throughout the entire interval of observation. Because the solution was well-constrained by this stage of the process using the March 18-25 data alone, the additional measurements from the side-on views from March 27-28 were primarily used to test the solution and to further fine-tune parameter values which were strongly interconnected, such as pole tilt and source latitude.

To emphasize the need for the very large, primary source region in successfully fitting the Hyakutake images obtained in late March with the model, we show in Figure 11 representative images from March 19, 24, and 28, compared with synthetic images obtained with our best solution, and with the best narrow-jet solution for March 24. As is readily evident, while the narrow jet solution works well on the 24th, the spacing of features is much poorer on the 19th, and does not fit at all on the 28th. In comparison, not only are jet features well-matched with the preferred wide jet solution on each night, but the overall coma intensity distribution is also significantly improved.

In this final stage of model fitting, we also utilized the overall brightness distribution in the images processed using the azimuthal median division method to constrain the relative amounts of material produced by each source. Not surprisingly, different model parameters were most strongly constrained with different parts of the data set. For instance, the outflow velocity was constrained best from the March 18-25 data, while the pole tilt was most tightly constrained using the March 27-28 data since a change in the tilt angle of the model produced a rotation of the line of symmetry in the comet's brightness on these dates. In a similar manner, the location of the observed secondary jet on March 27-28 could only be reproduced if the latitude of its model source was moved to a more-southerly value than was otherwise needed.

VII. MODEL RESULTS

Ultimately, our preliminary best solution was obtained with a primary source region even larger than we initially suspected, approximately 56° radius, centered at a latitude of about –66°. This solution was self-consistent in all respects except for one — the derived longitude of both the primary and secondary sources progressively shifted with time, with each decreasing by between 20 and 25° over the span of 10 days between the 18th and 28th. After confirming that this non-physical trend remained for any otherwise viable model solution, we next investigated if the observed trend was simply an artifact of using an incorrect rotation period for the nucleus. A net artificial longitude shift of 22° would imply a shift by slightly under 0.6° per rotation over the 38 rotational cycles covered by the dataset. This, in turn, implied that this artificial trend in longitude could be eliminated if a sidereal period of 0.2618 rather than 0.2614 day was utilized in the model, and testing confirmed this fact. Based on the trend removal, we estimate the uncertainty as ±0.0001 day.

The reason for this difference in the periods is very simple. The 0.2614 day (6.274 hr) period was derived by Schleicher and Osip (2002) from an analysis of the rotational lightcurve, and the amount of material released from the nucleus is driven by available solar radiation, with the corresponding amount of material within an observing aperture being nearly independent of viewing geometry. Therefore, the observed period is a solar or local synodic period (not to be confused with an asteroidal synodic period which does depend on the observer's location), and this value will change with the comet's orbital motion and with its pole orientation. In contrast, our Monte Carlo model uses an object's sidereal period in the calculations, which in principle remains constant throughout the orbit (ignoring possible changes caused by any torque produced by outgassing). Because the difference between the sidereal and solar periods depends on the pole orientation, we could not *a priori* assume the value of this difference. Once the pole position was determined, however, we could calculate the expected difference, and for our best pole solution the difference in late March is 0.0003 day. Because the pole tilt is >90°, the sense of rotation is retrograde with respect to the orbital motion (following the right-hand rule) and, therefore, the calculated solar period is shorter than the sidereal period, ie., 0.2615 day, nearly identical to the 0.2614±0.0004 day solar period derived by Schleicher and Osip.

Using the sidereal period of 0.2618 day for a final round of tweaking model parameters, our final best solution is given in Table III, where all positional values were determined to the nearest 2°. Our estimated uncertainties for the pole tilt, pole orbital longitude, and source latitudes and radii are each 3°, while source longitudes have uncertainties of about 5°. These estimates are based on the amount a parameter or combination of parameters could be changed before a noticeable degradation in the quality of the fit of the model to the image was apparent using our “by eye” technique. However, the derived source radii are strongly tied to the assumed dispersion in the outflow direction of the dust leaving the surface since, to first approximation, their affects on the jets’ appearance mimic each other. For instance, if there were no dispersion from the normal direction, rather than the assumed 5° Gaussian dispersion to the normal direction, then our best solution would require source radii about 5° larger than the values quoted above to keep the total jet width approximately constant. The reverse is also true, and a larger directional dispersion than the assumed 5° would require correspondingly smaller source radii. However, the radii cannot decrease arbitrarily small with an increase of directional dispersion, because some dust features observed in the data require that the primary source region extend to both low latitudes and “over” the pole to match the changing duration of sunlight available across the source region. While the specific solution listed in Table III obviously depends on our model assumptions of a spherical nucleus and circular source regions, there are clearly insufficient data to use more physically realistic nucleus model. To first approximation, the derived latitudes can be considered equivalent to effective latitudes on an elongated nucleus defined by normal directions on the surface.

Using our nominal dispersion and the resulting source radii of 56° and 16°, the primary and secondary source regions cover approximately 9100 degree^2 and 800 degree^2, or an 11:1 ratio, with the primary source encompassing approximately 22% of the total surface area of the nucleus, and the two sources combined covering about 24%. This result is in excellent agreement with the 20-25% active fraction estimated by Schleicher and Osip (2002) near perigee, based on the measured water production at this time and a nucleus radius of 2.4 km. This assumed radius value was a compromise between several measured values along with upper and lower limits (cf. Lisse *et al.* 1999 and Altenhoff *et al.* 1999). Because our modeling efforts made no assumption of the nucleus size, the resulting fractional area we compute from the jet modeling provides independent support that Hyakutake’s nucleus radius was indeed close to 2.4 km, which is consistent with the radar measurements only if the radar albedo was near 0.012, indicative of very lightly packed material (cf. Harmon *et al.* 1997).

The 11:1 ratio in relative areas of the two source regions was sufficiently close to the originally assumed particle distribution ratios of 80%:10% that we did not adjust the distribution values in our final solution. Moreover, a larger uncertainty exists regarding the assumed 10% fraction due to the third model component: particles released from the entire nucleus surface, providing an ambient background source. The ratios we assumed for the modeling were primarily based on the large amplitude of the rotational lightcurve and the general appearance and brightness of the jets to the background coma. We estimate that the isotropic component might be as high as 20% of the total; however, it could also be as low as 0%, since it is apparent from the modeling that the more diffuse background coma could be entirely explained by larger, slower-moving dust grains emitted by the two identified source regions. In any case, we are certain that the large majority of particles in Hyakutake’s coma were emitted by the primary source region.

Our modeling also shows that the dust velocity scaler, which allows for an additional possible projection effect on the projected velocity function derived in Section IV, has a value of unity. Our estimated uncertainty on this scaler is about 4%. The nominal particle size used in the model was about 2 microns, based on the observed radiation pressure effects. However, this effective radiation pressure is not well constrained due to the limited field of view of our imaging during Hyakutake’s close approach and the apparently abrupt start-up of radiation pressure effects on the dust jets at about 8000 km — no effects from radiation pressure were detected inside of 8000 km, but beyond this distance the dust was clearly slowed by radiation pressure. We attribute this behavior to the effects of collisions with the outflowing gas, as evidenced by the continued acceleration of dust to distances of ~4000-8000 km; until the dust was completely decoupled from the gas, the effects of collisions overwhelmed the competing acceleration from radiation pressure. Since we do not attempt to directly include collisions in our modeling, our adopted value for the effective particle size is simply a compromise which mimics the lack of observed radiation pressure effects prior to 8000 km, and cannot be used to derive the size of Hyakutake’s dust grains. Finally, we also tested our adopted functional form of the solar efficiency with sun angle for the release of grains from the surface. The assumed function, the cosine of the sun angle, was based simply on the concentration of solar radiation on a normal surface. However, if sunlight needs to penetrate into cracks and crevasses, then the appropriate function would need to be steeper than the cosine of the sun angle. Our testing showed that steeper functions, such as the cosine^2, yielded poorer fits overall than the adopted cosine function.

A detailed comparison of our best overall model solution with a corresponding image from March 24 is presented in Figure 12 in both sky plane and polar coordinate views. Jet measurements are included in each representation, and the model test particles are color-coded to distinguish between the jets. We consider this an excellent match between the model and the observation both in the location of the peak intensity along each jet as well as the general bulk asymmetries in brightness. In Figure 13, we show a variety of thumbnail sky plane image comparisons between observations and the model from the entire span of observations. The apparent bifurcation of features during their outward motion on March 27-28 is a natural consequence of the changing overlapping jets when seen from side-on. Synthetic model rotational cycle animations for March 24 and 28 are also presented on our web site.

Our pole solution, with an obliquity of 108° and orbital longitude of the pole of 228°, corresponds to an ecliptic latitude of +8.7° and ecliptic longitude of 203.9°, or an RA of 13^h41^m and Dec of –1.1°. We define this as the north pole, following the right-hand rule convention. In the rapidly changing view from Earth, the resulting apparent position of the north pole for our nights of observation are included in Table I, where the aspect angle is the projection with respect to the plane of the sky, and the pole orbital longitude is the apparent position angle of the rotation axis with respect to north on the plane of the sky. As indicated, the south pole of the nucleus pointed to within only 18° of Earth on March 20 before crossing the plane of the sky on March 27. By perihelion, the northern hemisphere of the nucleus would have dominated the view from Earth, with the north pole pointed only 23° from Earth.

To more effectively conceptualize Hyakutake's nucleus, we have also created synthetic views of our model nucleus by greatly reducing the time interval over which particles are emitted and forcing any particles not emitted to remain on a synthetic nucleus surface and then zooming in on this. We also hide particles on the far side of the nucleus, and hide most particles on the night hemisphere to effectively darken it, thereby making the terminator evident. In Figure 14 we show views of this model nucleus and the surrounding few kilometers for 4 equally-spaced rotational phases on March 24 as viewed from Earth. Immediately evident is the circumpolar region which releases material throughout the rotation cycle because it receives sunlight continually. A portion of the primary source also points towards Earth each rotation; hence, our view is from *within* the broad primary jet for a portion of each cycle. With a sub-Earth latitude of –45° on this date, the southern edge of the secondary source just misses sweeping across the Earth.

VIII. DISCUSSION

In the end, we were gratified that a relatively simple model having only two source regions provided a very good match to the observations over a wide range of viewing geometries. Very few compromises needed to be made in arriving at our final solution. For instance, while we certainly do not claim to have perfectly matched every image, our final solution does not show any systematic trends in the quality of the fit over the 11 night interval. The most significant deviations between the model and the actual images occurred on March 21 and 22, shortly after the on-set of the outburst, in which the measured jet locations were often at somewhat larger distances than predicted by the model over position angles of about 60-200°. We believe this was an artifact introduced by the excess material released in the outburst and the resulting effect on the radial profiles, since these deviations were not visible before or after these dates. Another noticeable departure of the model from the data occurred at a small range of rotational phases, when the detailed shape of the primary jet would differ from the model. These were most evident on March 23-24, were we had the most complete phase coverage. We also saw some evidence in the enhanced images for near-radial structures within the envelope of the primary jet on March 26-28. In both of these cases, we suspect that limitations caused by our model assumptions regarding the shape of the nucleus and/or the shape of each active region are to blame. While we adopted a spherical shape for the nucleus, it is highly unlikely that the nucleus has this shape. Indeed, all evidence points to comet nuclei often being greatly elongated, and possibly having very irregular surfaces with significant topographic features. Both of these possibilities would result in differing fractions of the surface having particular normal directions as compared to our assumed spherical nucleus, resulting in varying densities within a jet. Moreover, it is also unlikely that a source region is circular in extent. In fact, certain characteristics of the secondary jet's shape as a function of viewing geometry suggest that its source region might be elongated and oriented approximately north-south. For these reasons, overall we consider the lack of shape information for the nucleus as being the greatest source of uncertainty in these model results.

It has been suggested that small-sized nuclei might be expected to be in excited rotational states due to the torques caused by outgassing (cf. Jewitt 1999 and references therein). However, our good match to the observations over an 11-day interval provide evidence that Hyakutake's nucleus is not in a complex rotational state and does not experience strong precession. Any significant deviation from simple rotation would have been readily visible during the first 8 days of the interval, but the jets' appearance were essentially identical from one rotation cycle to the next, and the only systematic trend evident when a principle axis rotation model was used was resolved by a very small change in the assumed rotation period. Furthermore, the photometric lightcurve was also completely consistent with simple rotation (see Schleicher and Osip 2002). Therefore, while a long-period precession certainly cannot be ruled out, Hyakutake did not display any evidence in March 1996 which might be attributable to either significant precession or complex rotation.

Seasonal Effects

Our solution for the pole orientation and source locations can be used to investigate the relative r_H-dependence of water before perihelion (cf. Schleicher and Osip 2002), and the cause of the strong asymmetry observed in production rates pre- and post-perihelion in radio observations (Biver *et al.* 1999). Schleicher and Osip suggested that both of these observed effects might be due to seasonal changes. During the interval of our CCD observations, the sub-solar latitude was about –70°, nearly matching the location of the center of the primary active region (–66°). Therefore, we would expect that the efficiency of gas vaporization and dust release was near the maximum possible. This can be visualized by examining the synthetic nucleus in Figure 14. We can quantify this by examining the nominal amount of sunlight which was available when each test particle was released (or, if the sun were below the nominal horizon, the lack of sunlight resulting in the particle remaining on the surface). This is shown in Figure 15, where we plot the cosine of the sun angle for the particles which are successfully emitted from the surface (proportional to the cosine) as a function of rotational phase for March 24 and for May 1 (perihelion). In late March, neither source region ever shuts off completely because of the very southerly sub-solar latitude. However, by perihelion, only the northern-most sections of both sources are illuminated, and then for only part of the rotation cycle and with a low sun angle.

We can integrate this solar illumination function over an entire rotation cycle to compute the solar efficiency, and repeat the process as a function of time throughout the apparition. The result is presented in Figure 16 where we also plot the sub-solar latitude with time. Several seasonal effects are immediately evident in this figure. First, is the fact that the illumination is nearly unchanged during the months prior to perihelion, with the sub-solar latitude only beginning to rapidly approach the equator in the last half of April. Although Schleicher and Osip (2002) preferred a seasonal explanation to explain why the r_H-dependence of water production was lower than would be expected from a water vaporization model during this interval, over the alternative explanation of a significant icy grain source, our modeling implies that the low r_H-dependence was apparently not seasonal in nature. Furthermore, this result is largely independent of the specific functional form of the solar illumination function with sun angle. Schleicher and Osip had ruled out a distributed source because no trend was seen in the measured production rate of OH (the direct daughter of water) as a function of photometer aperture size. Since this constraint is still valid, we propose the following explanation: That icy grains provided a significant additional source of water, but that these grains vaporized within ~1000 km of the nucleus, and therefore did not have an affect on the measured spatial distribution of OH. This scenario also requires that the proportion of water released from grains vs vaporization of the nucleus decreased as Hyakutake approached the sun. This could be due to a series of outbursts or fragmentations throughout the comet's approach, only much smaller in scale than the outburst of late March. This possibility is supported by the fact that OH production, unlike most other species, did not show a trend with aperture size even during the outburst, when gas production doubled over baseline values, implying this excess OH was released directly from the outburst fragments or rapidly vaporizing icy grains released at this time. Unfortunately, we are unaware of any data sets which can directly test this hypothesis.

Returning to Figure 16, the solar efficiency reaches a minimum a few days after perihelion (also see bottom panel of Figure 15) when the sub-solar latitude very briefly reaches +72° as the comet rapidly swings around the sun. After this time, the sub-solar latitude progresses southward more slowly, nearly reaching the equator by mid-June. Because the sun remains in the northern hemisphere, the integrated solar illumination function never returns to pre-perihelion values, resulting in a large predicted asymmetry of dust and gas production rates about perihelion. The size of this asymmetry would be reduced if additional source regions exist on Hyakuake's nucleus north of +20°. In such a location, they would remain in the dark until after mid-April, and so would not produce detectable jets prior to this time. However, we are not aware of any imaging of the comet that was obtained after the third week of April, so a direct test of this possibility is also not feasible. Instead, a less direct check of our illumination function can be made. Although the only post-perihelion water production rate measurement is indeed lower than most pre-perihelion measurements (Gérard *et al.* 1998), the uncertainties in modeling this OH radio measurement dominates the resulting value. However, Biver *et al.* (1999) measured several other species in the radio, and they observed a strong asymmetry, with the values being at least 50% smaller on average after perihelion. When compared to the pre-perihelion heliocentric distance dependencies in production rates between mid-February and mid-April measured by Biver *et al.*, production rates of most of their observed species increased less than expected or even dropped beginning in the third week of April, and by April 27-29 (the only observations obtained within a week of perihelion) were as much as an order of magnitude lower than would otherwise have been expected based on the r_H-dependence measured previously for each species. Their results appear to be entirely consistent with what we expect from our integrated solar illumination function, providing support for our model solution and indirect evidence that there probably was not an additional major source region located in the northern hemisphere.

Dust Outflow Velocity

Returning to the topic of dust outflow in the innermost coma, we remind the reader that in Section IV we were able to utilize the jet positions as a function of rotation at different position angles to ultimately obtain a curve of the dust grains' distance vs time (Figure 8), normalized for differing projection effects with PA. This curve was then fit with a simple parabola, and used as an input to the Monte Carlo modeling, with an additional free parameter for scaling this result. In our best model solution, the value of this scaler was unity, implying that no remaining bulk projection effect on the derived curve, although our estimated uncertainty on this scaler is about 4%. (Larger and smaller scaler values resulted in systematic trends over the 11 nights.) The reason no bulk projection effect remained for the dust outflow velocities is a direct consequence of the very broad source region. Essentially, the peak in observed brightness is largely determined by jet material in the plane of the sky, as long as a portion of the jet lies in the plane of the sky. With a primary source diameter of ~110°, a portion of the jet fulfills this requirement during all but the last few nights of observations. In other words, the very nature of the broad jet projection effects which make the spiral appear nearly circular, i.e. face-on, even when the pole is not pointing directly toward the Earth, helps to minimize what would otherwise be larger projection effects in the measured positions and velocities of the jets.

A consequence of this is that the parabolic fit of the measured outflow of dust as a function of distance presented in the bottom panel of Figure 8 is also the fit to the true radial outflow. This curve is again shown in the top panel of Figure 17 on an expanded scale as a function of time from release of the grains. From this curve we can extract the velocity as a function of distance, and this is shown in the bottom panel. As we noted previously, we believe this is an excellent representation of the visible dust jet outflow characteristics to at least 4×10^3 km, and is consistent with the data out to 8×10^3 km, before radiation pressure effects begin to dominate. Because most, if not all of the dust was released from the identified source regions, this also characterizes the bulk outflow of dust in Hyakutake. Coupled with the excellent spatial resolution due to Hyakutake's close approach to Earth, this may be the first detailed measurement of the acceleration of dust grains in the inner-most coma as a function of distance from a comet's nucleus.

Early formulations of dust acceleration from the surface of a nucleus resulted in the dust essentially reaching terminal velocity within a few tens of the nucleus radius (Whipple 1951). Subsequent calculations have included the effects of gas acceleration, non-spherical grains, and heating of the gas by the grains, yielding values from a few hundred kilometers up to one or two thousand kilometers for the distance at which dust grains decouple from the outflowing gas (cf. reviews by Crifo 1991; Sekanina *et al.* 2001). In comparison, our data indicate that the terminal dust velocity was not reached until at least 4000 km, even though our largest velocity measured is similar to the terminal velocities predicted by these other coma models at much smaller distances. This difference in distances may be due to particular details regarding Comet Hyakutake — perhaps the dominant grain size is somewhat smaller and the grains are more porous or "fluffy", i.e. having much lower effective densities than have been usually assumed in these acceleration models (see Gustafson 1989). We certainly do not know if the velocity vs distance function we measure in Hyakutake is typical of other comets. However, in general the gas density only drops as $1/r^2$, and the actual collision rate drops even less rapidly since the outflowing gas continues to accelerate within this regime. We measure the CN gas jets in Hyakutake (which we will examine in detail in a subsequent paper) to have more than twice the velocity of the dust, so collisions by the gas will always tend to accelerate the dust, even if by only a small amount. An analogous situation existed for investigations of collisional quenching of the radio OH lines. For many years, investigators analyzed their OH observations using the assumption that a quenching radius separated the OH into two regimes — inside the radius all OH molecules were quenched, while those molecules outside this radius were unquenched — similar to the concept of a Strömgren sphere for ionized nebula, where there is a sharp transition at the Strömgren radius from ionized to neutral hydrogen. It was later shown by Schloerb (1988) that the transition zone between the fully quenched regime and the unquenched regime is actually very much larger than assumed — typically more than 10^5 km. Our measured dust jet velocities in the interval between ~500 and 8000 km suggest a similar scenario for dust collisions, but on a much smaller scale. Therefore, a more realistic picture of dust acceleration may involve a slower drop off in the outflow acceleration of the dust, only gradually reaching a true terminal velocity thousands of kilometers further away from the nucleus than has previously been assumed.

IX. SUMMARY

Comet Hyakutake was an ideal candidate for the first successful application of our Monte Carlo jet model. The orbital path and short rotational period allowed us to collect images over many rotational cycles and over a wide range of viewing geometries in just a few nights, permitting a thorough test of the model itself as well as our final fit parameters. Only two source regions were required to fit the data, and the pole orientation and source region locations both successfully reproduce the observed morphology and explain the observed seasonal effects. It is evident from these results that while narrow jets emitted by small source regions can reproduce the observed morphology for individual viewing geometries, source regions of considerable extent which produce broad jets are essential to explain Hyakutake's dust morphology over time. Based on this result, we confirm the suggestion by Samarsinha (2000) that extended sources must be considered when modeling cometary jets. Our modeling also tightly constrained Hyakutake's sidereal rotation period as 0.2618±0.0001 day, a value which, given the pole orientation and position of the comet in its orbit, is completely consistent with the expected +0.0003 day difference from the observed solar rotation period of 0.2614±0.0004 day (Schleicher and Osip 2002). Additionally, we measured multiple fragments moving down the tail, with most of our results in excellent agreement with those of Desvoivres *et al.* (2000). The partial fragmentation of comets is probably a common occurrence, which was easily detected in Hyakutake due to the high spatial resolution. Finally, we find that the dust in this comet was still accelerating well beyond the region where most models in the past have assumed it should have reached terminal velocity. While it is possible that Hyakutake had unusually light or fluffy dust grains, it is certainly true that future modeling efforts should not simply assume that a comet's dust has reached terminal velocity within a few hundred kilometers of the nucleus.

ACKNOWLEDGEMENTS

We gratefully acknowledge the assistance of B. Skiff, M. Buie, D. Osip, R. Millis, L. Wasserman, and S. Lederer in the acquisition of many of the reported observations, and C. Eberhardy, D. Douglas, M. O'Hara, and R. Greer with data reductions. We particularly thank T. Farnham for his assistance in the development of the Monte Carlo model including the implementation of the many coordinate transformations, as well as innumerable discussions regarding the modeling and other aspects of this research. We also acknowledge the excellent exploratory data analysis software package DataDesk from Data Description, Inc., within which we developed our Monte Carlo comet jet model. This work was funded by NASA Grants NAG5-7947 and NAG5-9009.

REFERENCES

Altenhoff, W. J., J. H. Bieging, B. Butler, H. M. Butner, R. Chini, C. G. T. Haslam, E. Kreysa, R. N. Martin, R. Mauersberger, J. McMullin, D. Muders, W. L. Peters, J. Schmidt, J. B. Schrami, A. Sievers, P. Stumpff, C. Thum, A. von Kap-herr, H. Wiesemeyer, J. E. Wink, and R. Zylka 1999. Coordinated radio continuum observations of comets Hyakutake and Hale-Bopp from 22 to 860 GHz. *Astron. & Astrophys.* **348**, 1020-1034.

Biver, N., D. Bockelée-Morvan, J. Crovisier, J. K. Davies, H. E. Matthews, J. E. Wink, H. Rauer, P. Colom, W. R. F. Dent, D. Despois, R. Moreno, G. Paubert, D. Jewitt, and M. Senay 1999. Spectroscopic monitoring of Comet C/1996 B2 (Hyakutake) with the JCMT and IRAM radio telescopes. *Astron. J.* **118**, 1850-1872.

Boehnhardt, H. 2001. The death of a comet and the birth of our Solar System. *Science* **292**, 1307-1309.

Boehnhardt, H. and O. Barnbandner 1996. CCD observations of Comet C/1996 B2 (Hyakutake). *I.A.U. Circ.* **6364**.

Chernova, G. P., M. Ahmedzyanov, and N. N. Kiselev 1994. Photometry and polarimetry of comet Shoemaker-Levy 1991a1. *Planetary and Space Sciences* **42**, 623-625.

Crifo, J. F. 1991. Hydrodynamic models of the collisional coma. *In Comets in the Post-Halley Era.* (R. L. Newburn, Jr., M. Neugebauer, and J. Rahe, Eds.), Vol. 2, pp. 937-989. Kluwer Academic Publishers, Dordrecht.

Desvoivres, E., J. Klinger, A. C. Levasseur-Regourd, and G. H. Jones 2000. Modeling the dynamics of cometary fragments: Application to Comet C/1996 B2 Hyakutake. *Icarus* **144**, 172-181.

Desvoivres, E., J. Klinger, A. C. Levasseur-Regourd, J. Lecacheux, L. Jorda, A. Enzian, F. Colas, E. Frappa, and P. Laques 1999. Comet C/1996 B2 Hyakutake: Observations, interpretation and modelling of the dynamics of fragments of cometary nuclei. *Mon. Not. Roy. Astron. Soc.* **303**, 826-834.

Farnham, T. L., D. G. Schleicher, W. R. Williams, B. R. Smith 1999. The rotation state and active regions of Comet Hale-Bopp (1995 O1). *B.A.A.S.* **31**, 1120.

Farnham, T. L., D. G. Schleicher, L. M. Woodney, B R. Smith, W. R. Williams, E. A. Blount, E. Ford, S. M. Lederer, P. V. Birch, and C. C. Cheung 2002. The nucleus and coma morphology of Comet Hale-Bopp: A comprehensive model of the rotation state, active regions and emission velocities. In preparation.

Gérard, E., J. Crovisier, P. Colom, N. Biver, D. Bockelée-Morvan, and H. Rauer 1998. Observations of the OH radical in comet C/1996 B2 (Hyakutake) with the Nancay radio telescope. *Planetary and Space Sciences* **46**, 569-577.

Gonzalez, R.C. and R.E. Woods 1992. *Digital Image Processing.* Addison-Wesley Pub. Co.

Gustafson, B. A. S. 1989. Comet ejection and dynamics of nonspherical dust particles and meteoroids. *Astrophys. J.* **337**, 945-949.

Harmon, J. K., S. J. Ostro, L. A. M. Benner, K. D. Rosema, R. F. Jurgens, R. Winkler, D. K. Yeomans, D. Choate, R. Cormier, J. D. Giorgini, D. L. Mitchell, P. W. Chodas, R. Rose, D. Kelley, M. A. Slade, and M. L. Thomas 1997. Radar detection of the nucleus and coma of comet Hyakutake (C/1996 B2). *Science* **278**, 1921.

Harris, W. M., F. Scherb, J. W. Percival, K. Nordsieck, B. E. A. Mueller, D. Harmer, and A. Macdonald 1996. Imaging of Comet C/1996 B2 (Hyakutake). *I.A.U. Circ.* **6360**.

Jewitt, D. 1997. Cometary rotation. *Earth Moon & Planets* **79,** 35-53.

Jorda, L., J. Lecacheux, and F. Colas *et al.* 1996. Imaging of Comet C/1996 B2 (Hyakutake). *I.A.U. Circ.* **6344**.

Kidger, M. 2000. The disruption of Comet C/1999 S4 (LINEAR). *I.A.U. Circ.* **7467**.

Lecacheux, J., E. Frappa, P. Laques, F. Colas, L. Jorda 1996b. Comet C/1996 B2 Hyakutake. *I.A.U. Circ.* **6367**.

Lecacheux, J., L. Jorda, A. Enzian, J. Klinger, F. Colas, E. Frappa, and P. Laques 1996a. Comet C/1996 B2 Hyakutake. *I.A.U. Circ.* **6354**,

Lisse, C. M., Y. R. Fernández, A. Kundu, M. F. A'Hearn, A. Dayal, L. K. Deutsch, G. G. Fazio, J. L. Hora, and W. F. Hoffmann 1999. The nucleus of Comet Hyakutake (C/1996 B2). *Icarus* **140**, 189-204.

Millis, R., D. Schleicher, and L. Wasserman 1996. Photometry of Comet C/1996 B2 Hyakutake. *I.A.U. Circ.* **6372**.

Samarasinha, N. H. 2000. The coma morphology due to an extended active region and the implications for the spin state of Comet Hale-Bopp. *Astrophys. J.* **529**, L107-L110.

Schleicher, D. G., T. L. Farnham, B. R. Smith, E. A. Blount, E. Nielsen, S. M. Lederer 1998b. Nucleus properties of Comet Hale-Bopp (1995 O1) based on narrowband imaging. *B.A.A.S.* **30**, 1063-1064.

Schleicher, D. G., R. L. Millis, D. J. Osip, and S. M. Lederer 1998a. Activity and rotation period of Comet Hyakutake (1996 B2). *Icarus* **131**, 233-244.

Schleicher, D. G., and D. J. Osip 2002. Long and short-term photometric behavior of Comet Hyakutake (1996 B2). *Icarus*, in press.

Schleicher, D., D. Osip, and S. Lederer 1996. Photometry of Comet C/1996 B2 Hyakutake. *I.A.U. Circ.* **6372**.

Schloerb, F. Peter. 1988. Collisional quenching of cometary emission in the 18 centimeter OH transitions. *Astrophys. J.* **332**, 524-530.

Sekanina, Z., M. S. Hanner, E. K. Jessberger, and M. N. Fomenkova 2001. Cometary dust. In *Interplanetary Dust.* (E. Grun, B. A. S. Gustafson, S. Dermott, and H. Fechtig, Eds.) Springer Verlag.

Tozzi, G. P., and J. Licandro 2001. Visible and infrared images of C/1999 S4 (LINEAR) during the disruption of its nucleus. Submitted to *Icarus.*

Tozzi, G.-P.,F. Lisi, E. Oliva, and P. Patriarchi 1996. IR observations of Comet C/1996 B2 Hyakutake. *I.A.U. Circ.* **6357**.

Weaver, H. A. 1996. HST observations of Comet C/1996 B2 Hyakutake. *I.A.U. Circ.* **6363**.

Weaver, H. A., Z. Sekanina, I. Toth, C. E. Delahodde, O. R. Hainaut, P. L. Lamy, J. M. Bauer, M. F. A'Hearn, C. Arpigny, M. R. Combi, J. K. Davies, P. D. Feldman, M. C. Festou, R. Hook, L. Jorda, M. S. W. Keesey, C. M. Lisse, B. G. Marsden, K. J. Meech, G. P. Tozzi, R. West 2001. HST and VLT investigations of the fragments of Comet C/1999 S4 (LINEAR). *Science* **292**, 1329-1333.

West, R. M., and O. Hainaut 1996. Comet C/1996 B2 Hyakutake. *I.A.U. Circ.* **6343**.

Whipple, F. L. 1951. A comet model. II. Physical relations for comets and meteors. *Astrophys. J.* **113**, 464-474.

FIGURE CAPTIONS

Figure 1. The rotational phase of each dust image as a function of time. Note the nearly complete phase coverage on March 23-25 and 28. Our best solution for the sidereal period is used, 0.2618 day, with zero phase defined as the time of perihelion, May 1.395. Shaded symbols indicate images which are shown in one or more figures of this paper.

Figure 2. Representative dust image from March 25 shown with a variety of image enhancement techniques. All enhancement methods remove the bulk radial fall-off in intensity. Ultimately, the median stack enhancement technique was used on nights with complete or nearly complete rotational coverage to remove sunward/tailward asymmetries and the dust tail, yielding the maximum visibility of the jets. The azimuthal median technique was used on all nights; while similar to the $1/\rho$ removal technique for dust, it provided slightly better contrast than $1/\rho$, and also worked well with gas images. The Butterworth filter technique was used exclusively to measure the position of outburst fragments along the tail. See text for further details.

Figure 3. A representative dust image from each night, after enhancement using the azimuthal median technique. Each frame is 2×10^4 km on a side, with north at the top and east to the left. The changing viewing geometry progresses from nearly face-on spiral jets on March 18 to a side-on view with the sun nearly in the plane of the sky on March 28. The apparent position angle of the sun (opposite of the observed dust tail) also changes by about 230° during this interval. Note the motion of dust along the tail following the major outburst estimated to have begun on March 19.9 (see Schleicher and Osip 2002).

Figure 4. Representative polar coordinate images from each night, along with associated radial profiles. Each ρ vs PA plot was extracted from the corresponding image from Figure 3. Three curves are plotted for each radial profile plot: the azimuthal median (solid), the tailward 10° wedge (dashed), and a normalized $1/\rho$ profile (dotted). Note that the outburst is first detected on March 20, where there is a more than 2× increase in flux at $\rho < 10^3$ km, but is effectively removed by the azimuthal median enhancement. By the 21st, dust has moved down the tail sufficiently to easily be detected, and its motion can be followed over the next several days until it has almost completely dispersed.

Figure 5. A representative extracted tail image for each night from March 25-28, using the Butterworth filter enhancement technique described in the text. Each sub-frame is oriented with the anti-sunward direction to the right and the position of the nucleus at the left-hand edge. The location of the major outburst fragments are indicated by arrows. Of course, the actual fragments are not visible, but rather each acts like a mini-nucleus and is surrounded by the observed mini-coma.

Figure 6. Cometocentric distances of outburst fragments as a function of time. Distances are deprojected, having corrected for the phase angle of the sun and knowing that the fragments are moving directly anti-sunward. Filled symbols represent fragments detected on multiple nights while open symbols are of fragments only clearly detected on a single night. Fragments “A,” “B,” “C,” “D,” and “F” are fit by curves assuming constant acceleration along the tail; the fit to fragment A is heavily influenced by the measurements obtained prior to the 24th by Desvoivres *et al.* (2000). In addition, fragments “B” and “D” and the corresponding fits are in excellent agreement with measurements and fits by Desvoivres *et al.* The derived coefficients, time of separation (T_0) and non-gravitational acceleration (a), for the five fitted curves are listed in Table II.

Figure 7. Rotational phase sequences from March 24 and 28, enhanced with the median stack technique to emphasize the detailed jet structure. North is at the top and east is to the left. At one-quarter cycle intervals,

the average spacing between images is 1 hr 34 min; phase coverage is incomplete on the 28th. Near phase 0.0, the primary jet of a new cycle is located within 2000 km of the nucleus, while the same jet from the previous cycle is located beyond about 5000 km. The much fainter secondary jet first becomes visible near phase 0.5 on the 24th and is too faint and diffuse to be detected only one-half cycle later. In comparison, multiple cycles of the secondary jet are visible at all rotational phases on the 28th when it is viewed side-on. For instance, the outward moving arcs in the lower-left quadrant of each frame on the 28th are alternately caused by the primary and secondary jets seen in projection. Video loops of the rotation sequences are available from the research page at www.lowell.edu.

Figure 8. The projected distance of the dust jets as a function of time on March 24. In the top panel, all measurements for both jets are displayed, after adjusting the times by an integer number of rotational cycles to form a broad composite curve for each jet. Different symbols distinguish the PAs in groups of 60°. Note the variation in slope and/or time with changing PA. In the middle and bottom panels, the projected distances have been scaled so that the adjusted data between 3000 and 8000 km at each PA has an average slope of 0.38 km s^{-1}, the maximum well-determined average velocity in this distance range for any PA (see Figure 9). Scaled data are only shown for the primary jet for PAs with sufficient data to determine a curve out to 8000 km, i.e. those PAs highlighted in Figure 9. In the bottom panel, each curve from the middle panel has been shifted in time to obtain a single composite curve which best represents the outflow of dust from the nucleus. A second-order polynomial fit to these data is overlaid, excluding points beyond 8000 km where radiation pressure effects dominate.

Figure 9. The mean projected dust velocities of the primary jet for 3000 km > ρ > 8000 km as a function of position angle on March 24. These values are extracted from the top panel of Figure 8. Filled symbols correspond to PAs for which there are sufficient data to determine the primary jet's position as a function of time out to 8000 km, and are therefore included in the composite curve shown in the middle and bottom panels of Figure 8. The dashed line at 0.38 km corresponds to the maximum, well-determined velocity, while lower values are assumed to reflect additional projection effects at these other PAs.

Figure 10. Monte Carlo jet simulation for Comet Hyakutake on March 24, showing the projection effects introduced as the primary source region increases in radius from 5° (left) to 30° (center) and 56° (right); for clarity, the secondary jet is not shown here. The pole orientation and source location are fixed for each simulation to our best solution in the right-hand panel, with the primary source covering nearly one-quarter of the surface of the nucleus. In each case, a $1/\rho$ brightness fall-off has been removed from the model.

Figure 11. Representative images from March 19, 24, and 28, compared with synthetic images using our best overall solution (left) and with the best narrow jet solution from March 24 (right). North is at the top and east is to the left in these and all other images in the following figures. The measured jet locations extracted from the radial profiles (see section IV) are shown on the enhanced images and both synthetic model images, which were processed with a $1/\rho$ brightness fall-off removal. Note that the best solution yields good matches to the location and widths of the jets, the brightnesses along and between jets, and the overall sunward/tailward asymmetries. In comparison, the narrow (5°) jet solution fitted to the 24th yields poor fits on the other nights; *no* narrow jet solution matched the observations throughout the interval.

Figure 12. A representative image from the 24th (phase=0.73) shown as seen in the sky plane and the polar coordinate equivalent (left), and the corresponding best overall model solution. The measured jet locations are shown in each view. A $1/\rho$ brightness fall-off has been removed from the model to mimic the image processing applied to the CCD frame. The polar plots were particularly useful in constraining the detailed shape and curvature of the jets. This best solution was obtained by fine-tuning the ensemble of model parameters to match the dust images throughout the 11 nights and all rotational phases.

Figure 13. Representative images throughout the 11-night interval with the corresponding synthetic model for each image. For the synthetic model images, the particles emitted by the primary jet are color-coded as blue, the secondary jet as magenta, and the ambient background emission as yellow. This sampling shows a variety of rotational phases, and several specific phases at differing viewing geometries. The circular feature observed near the perimeter of several of the processed frames is an artifact of the azimuthal median processing technique caused by the comet being too close to the edge of the CCD on one or more frames used to create the master frame. We do not attempt to recreate the dust tail in the model, which is presumably composed of relatively large dust grains, most of which were released during the outburst.

Figure 14. The synthetic nucleus of Hyakutake shown at 4 equally-spaced (clockwise) rotational phases for March 24. With a solar phase angle of 50° and PA of 38°, the terminator can be seen in the lower-right quadrant of the nucleus. With a sub-solar latitude of –71°, all but the near-equatorial portions of both active regions receive sunlight throughout the rotational cycle. Hyakutake's north pole has a PA of 202° and an aspect angle of 135°, i.e. pointing 45° behind the viewing plane.

Figure 15. The solar illumination function for a single rotational cycle on March 24 (top) and at perihelion, May 1 (bottom). This shows the available solar radiation for each test particle which was emitted from the surface; the cosine of the zenith distance is also used to determine the probability that an individual particle is emitted, causing the decrease in density from the top down to the dashed line at zero, where the sun would have been at the local horizon. Below this, a small fraction of particles are emitted to act as tracers of the function for each jet assuming some thermal lag exists. The width of the band for each jet is a reflection of the size of the source region. At perihelion, the subsolar latitude is about +40° (see Figure 16), resulting in most of the primary source region receiving little or no sunlight.

Figure 16. Solar illumination as a function of time from perihelion (May 1.394) for the apparition. The sub-solar latitude (top) only begins to change significantly in April, and reached extreme values of –72° on March 8 and +72° on May 6. The illumination efficiency (bottom) is the fraction of the model test particles emitted during each rotational cycle, where 80% of all test particles are assumed to originate from the primary source region, 10% from the secondary source, and 10% are distributed uniformly over the entire surface. Only very small portions of each of the two source regions receives sunlight during the first half of May.

Figure 17. The radial distance of the dust from the nucleus as a function of time (top) and the outflow velocity as a function of radial distance (bottom). The distance vs. time is simply the 2nd order polynomial fit to the scaled measurements previously shown in the bottom panel of Figure 8. Beyond about 4000 km, the data can also be fit with a straight line. The velocity vs. distance curve was created by extracting the instantaneous slopes of the curve in the top panel. Note that the dust does not reach a terminal velocity within a few hundred kilometers, but continues to accelerate to at least 4000 km, most likely caused by much lower individual particle densities than is usually assumed, due to the grains being very porous or "fluffy."

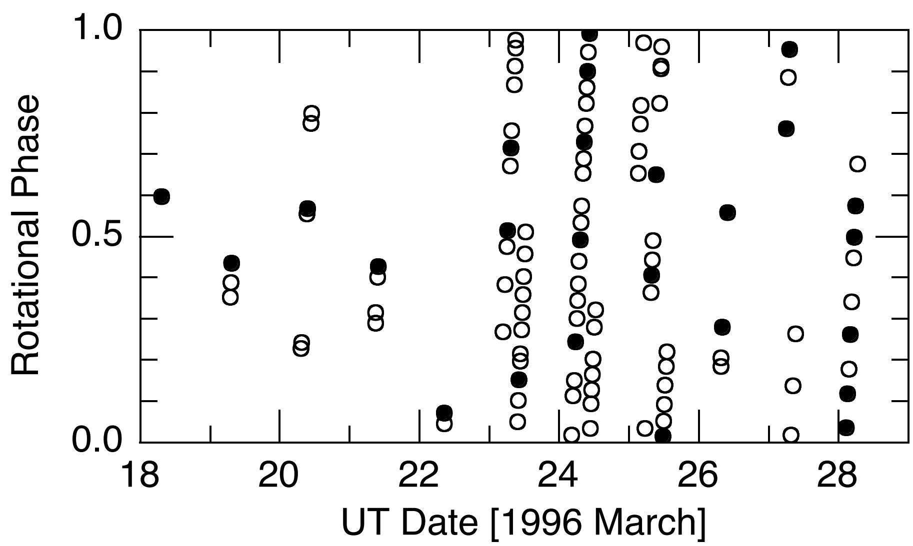

Figure 1

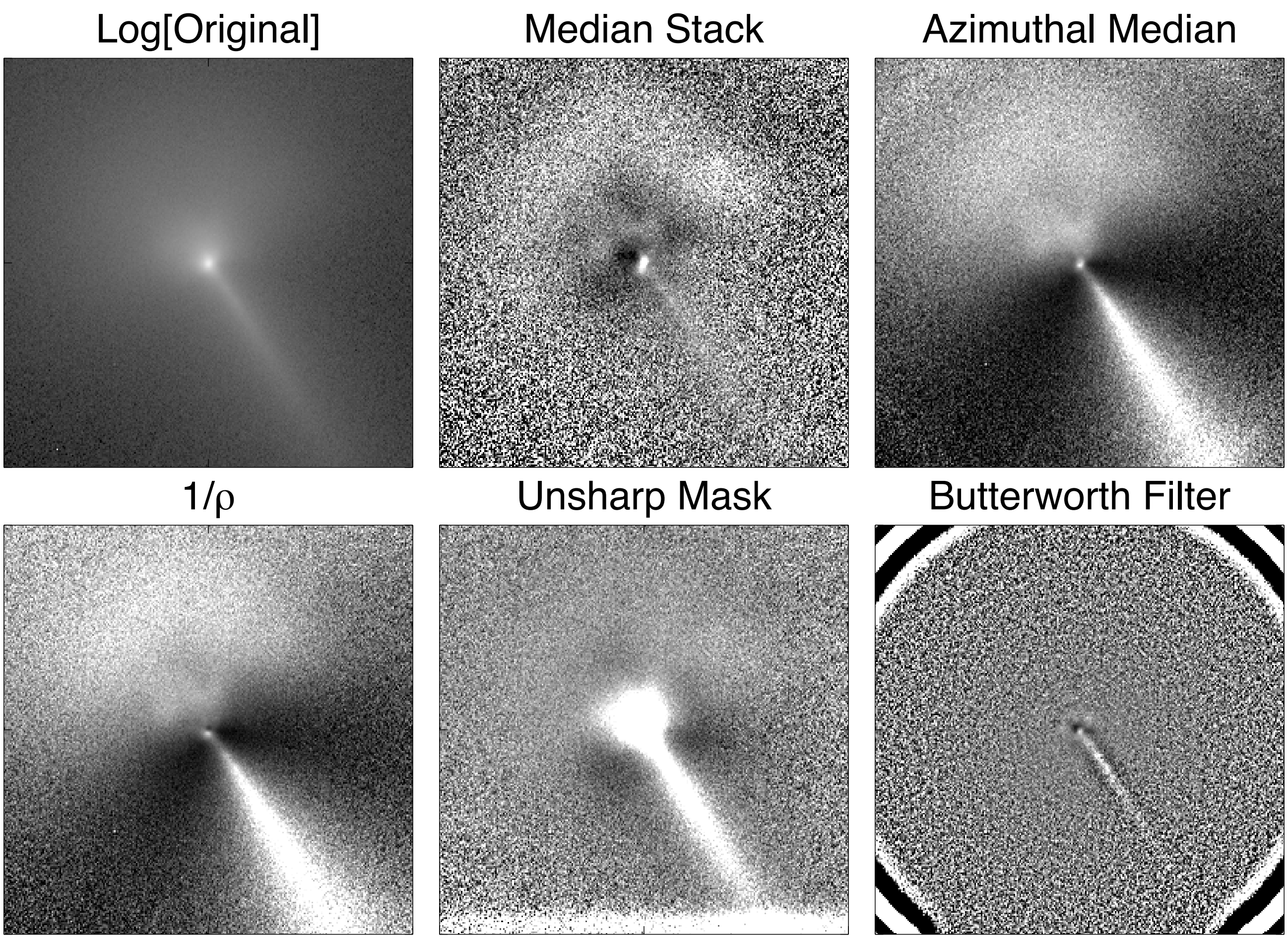
Log[Original]
Median Stack
Azimuthal Median
1/ρ
Unsharp Mask
Butterworth Filter

Figure 2

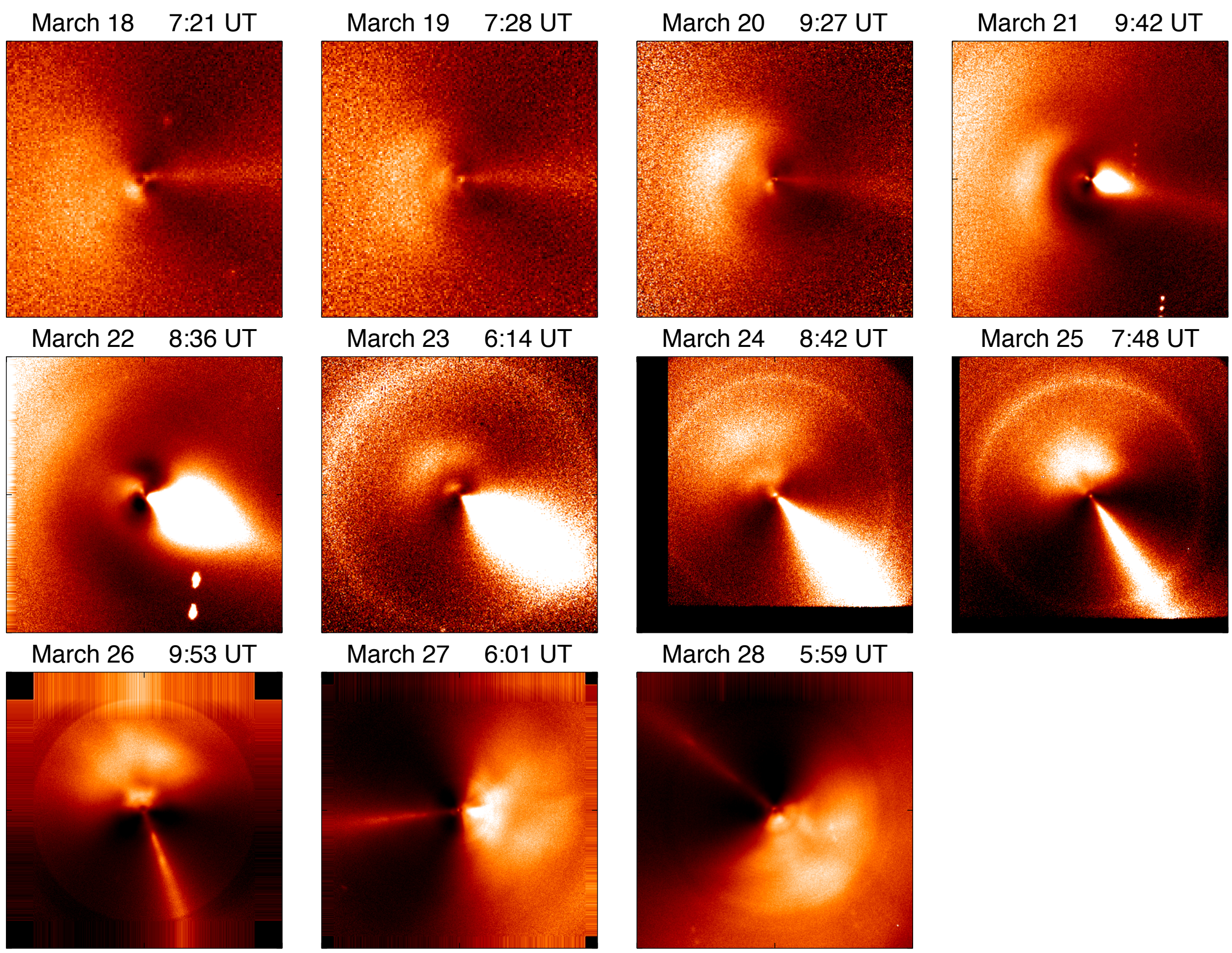
March 18 7:21 UT
March 19 7:28 UT
March 20 9:27 UT
March 21 9:42 UT
March 22 8:36 UT
March 23 6:14 UT
March 24 8:42 UT
March 25 7:48 UT
March 26 9:53 UT
March 27 6:01 UT
March 28 5:59 UT

Figure 3

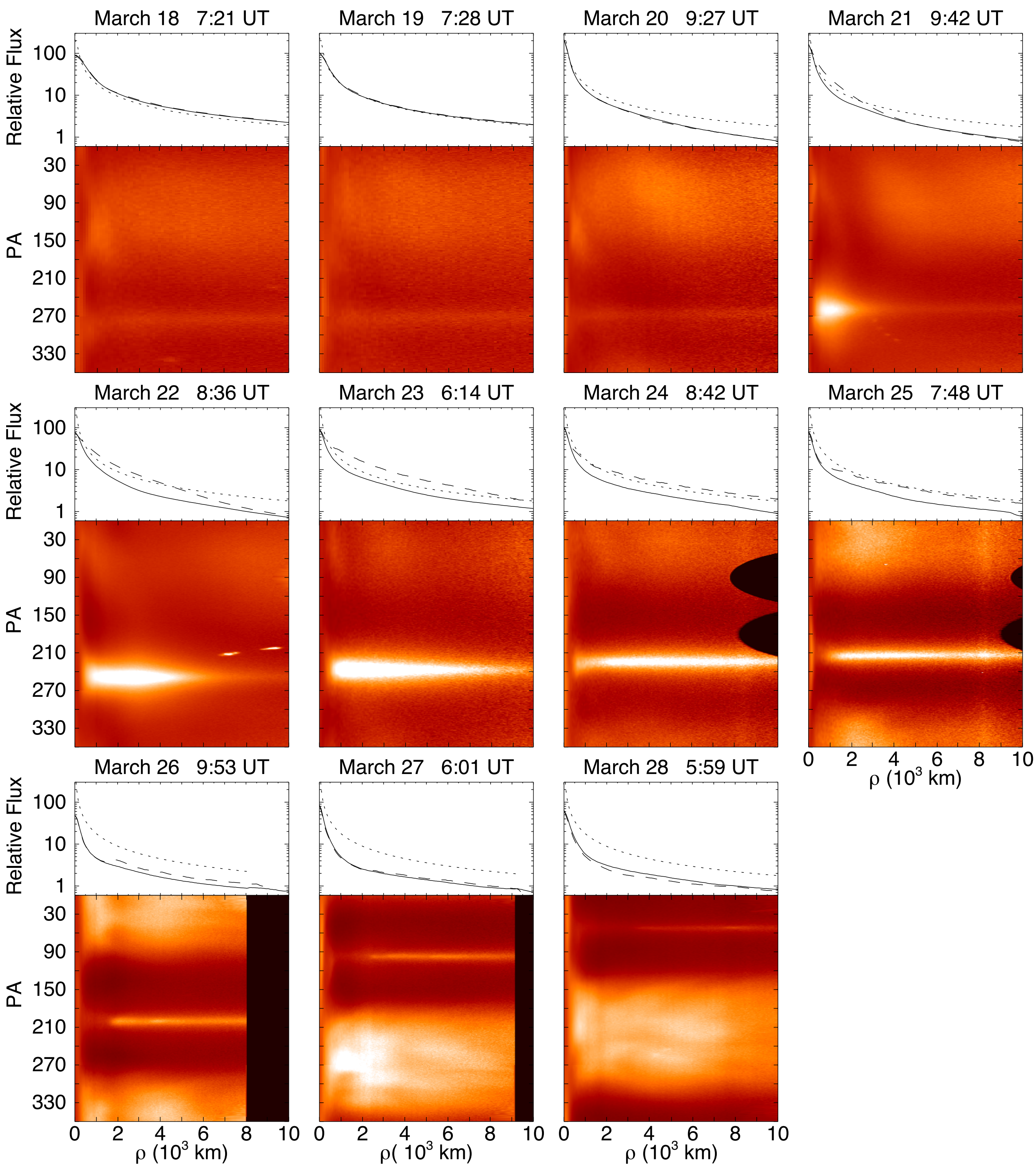

March 18 7:21 UT
March 19 7:28 UT
March 20 9:27 UT
March 21 9:42 UT
March 22 8:36 UT
March 23 6:14 UT
March 24 8:42 UT
March 25 7:48 UT
March 26 9:53 UT
March 27 6:01 UT
March 28 5:59 UT
Relative Flux
PA
ρ (10³ km)

Figure 4

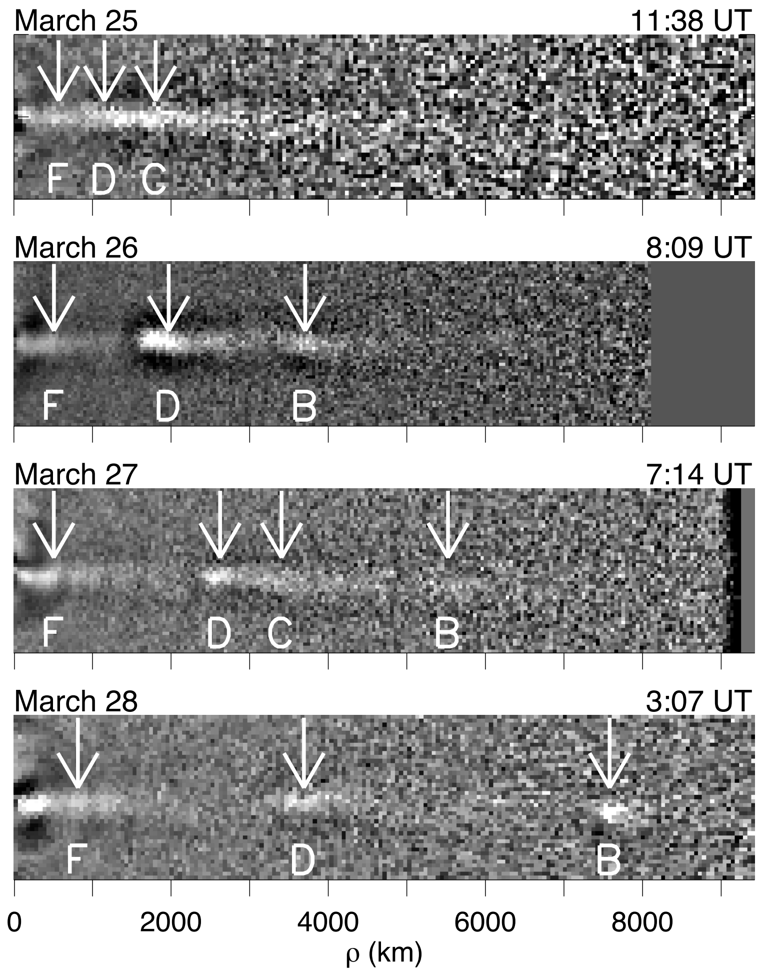
March 25
11:38 UT
F
D
C
March 26
8:09 UT
F
D
B
March 27
7:14 UT
F
D
C
B
March 28
3:07 UT
F
D
B
0
2000
4000
6000
8000
ρ (km)

Figure 5

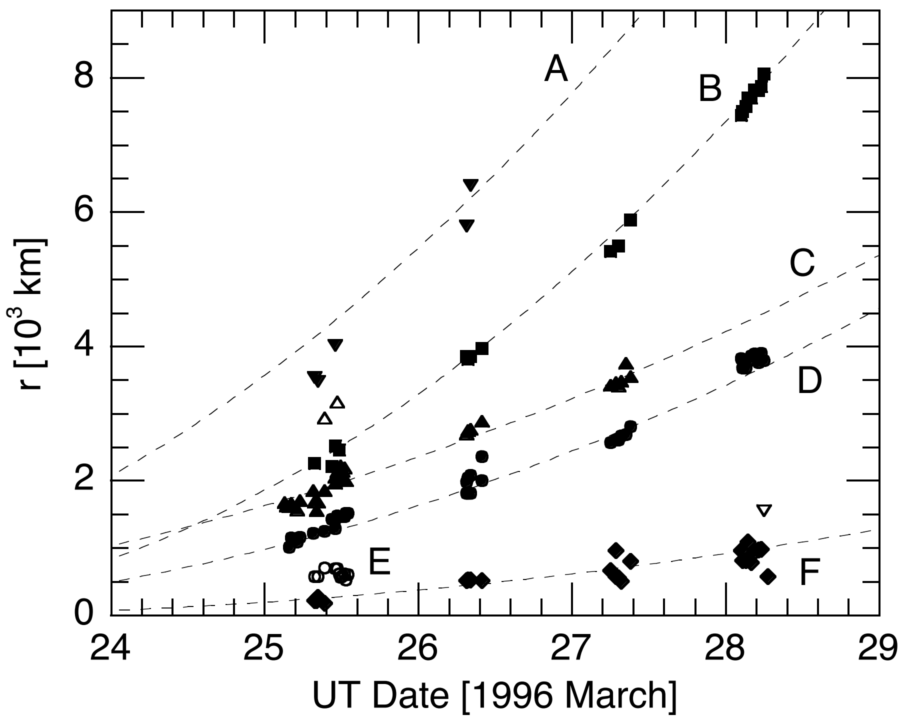

Figure 6

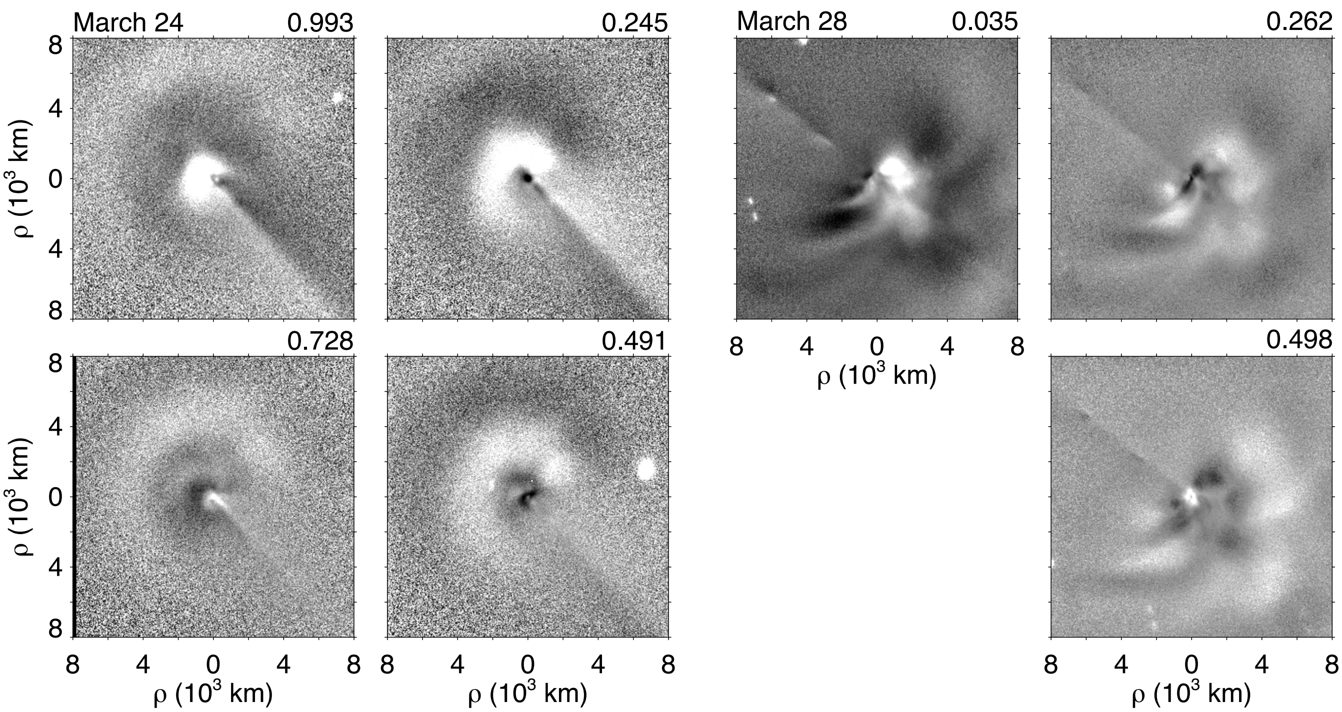

Figure 7

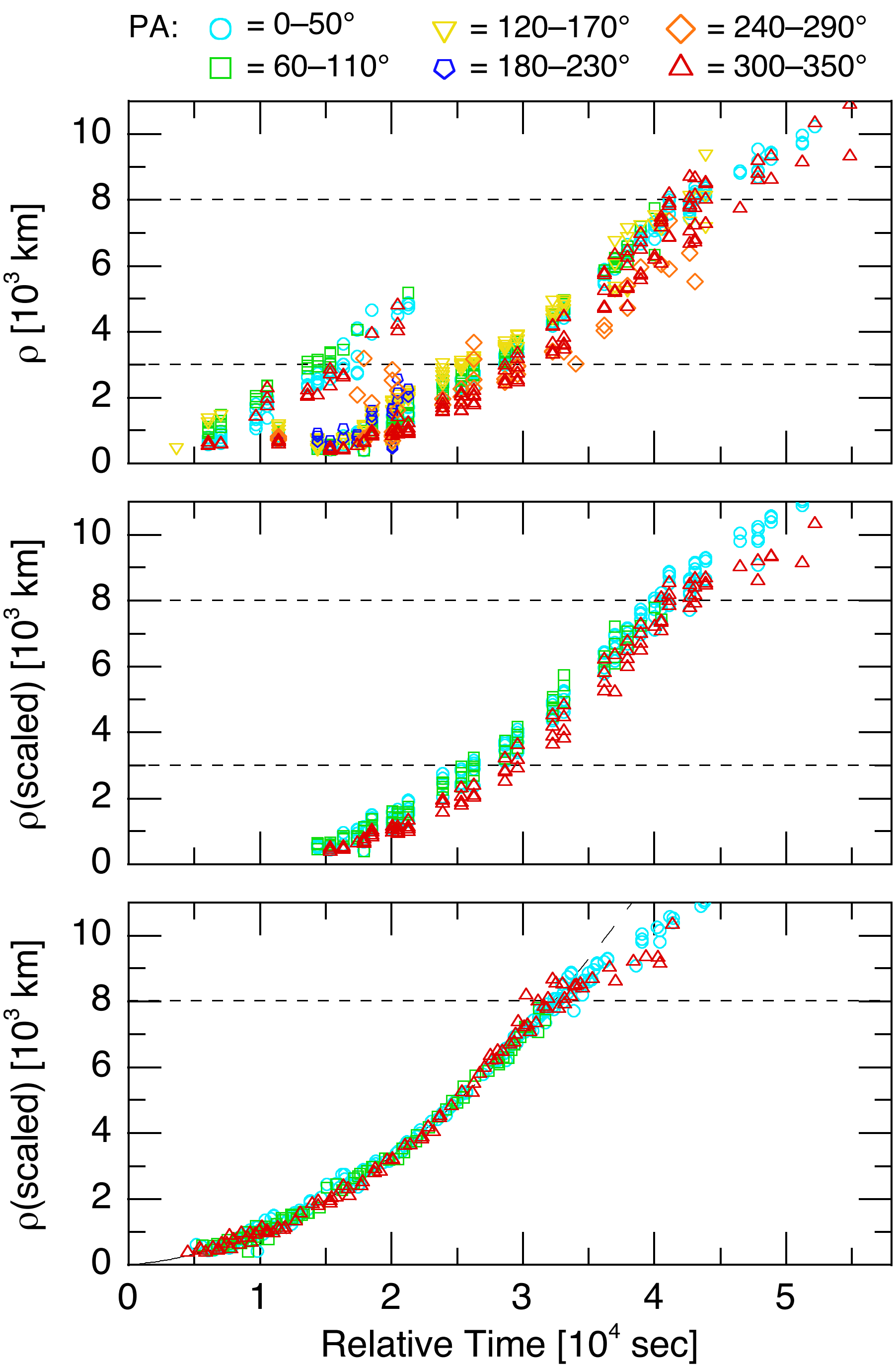

PA:
= 0–50°
= 60–110°
= 120–170°
= 180–230°
= 240–290°
= 300–350°
ρ [10³ km]
ρ(scaled) [10³ km]
ρ(scaled) [10³ km]
Relative Time [10⁴ sec]

Figure 8

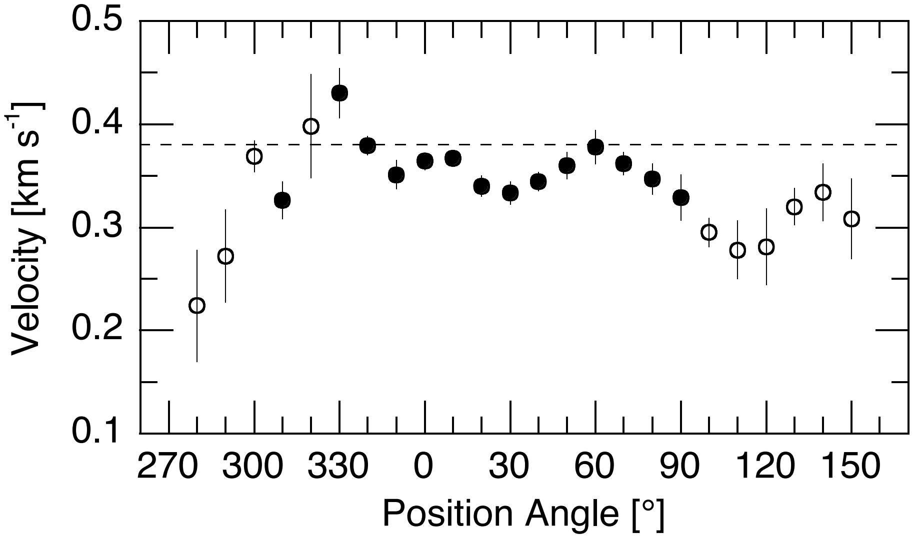

0.5
0.4
0.3
0.2
0.1
Velocity [km s-1]
270
300
330
0
30
60
90
120
150
Position Angle [°]

Figure 9

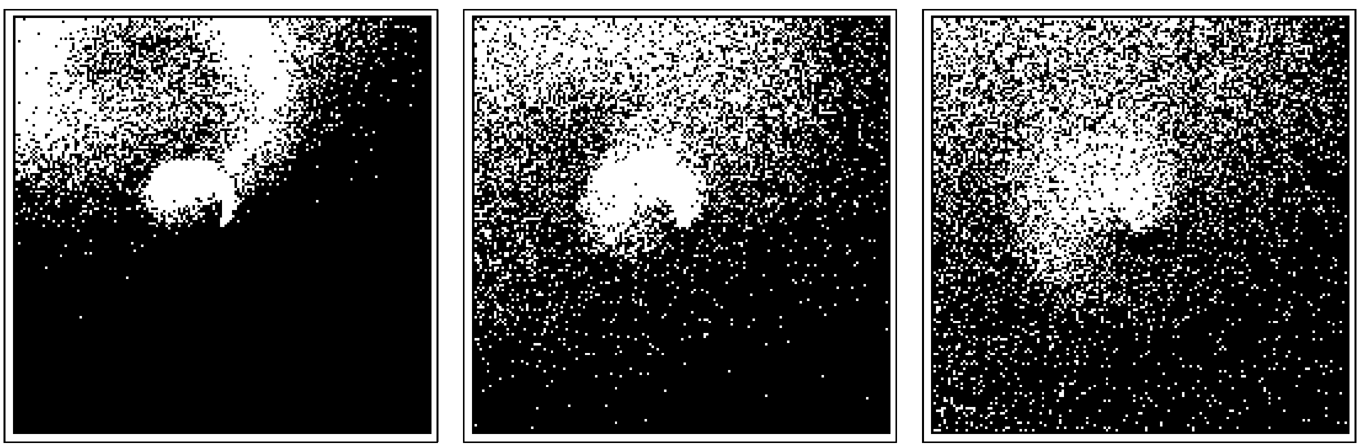

Figure 10

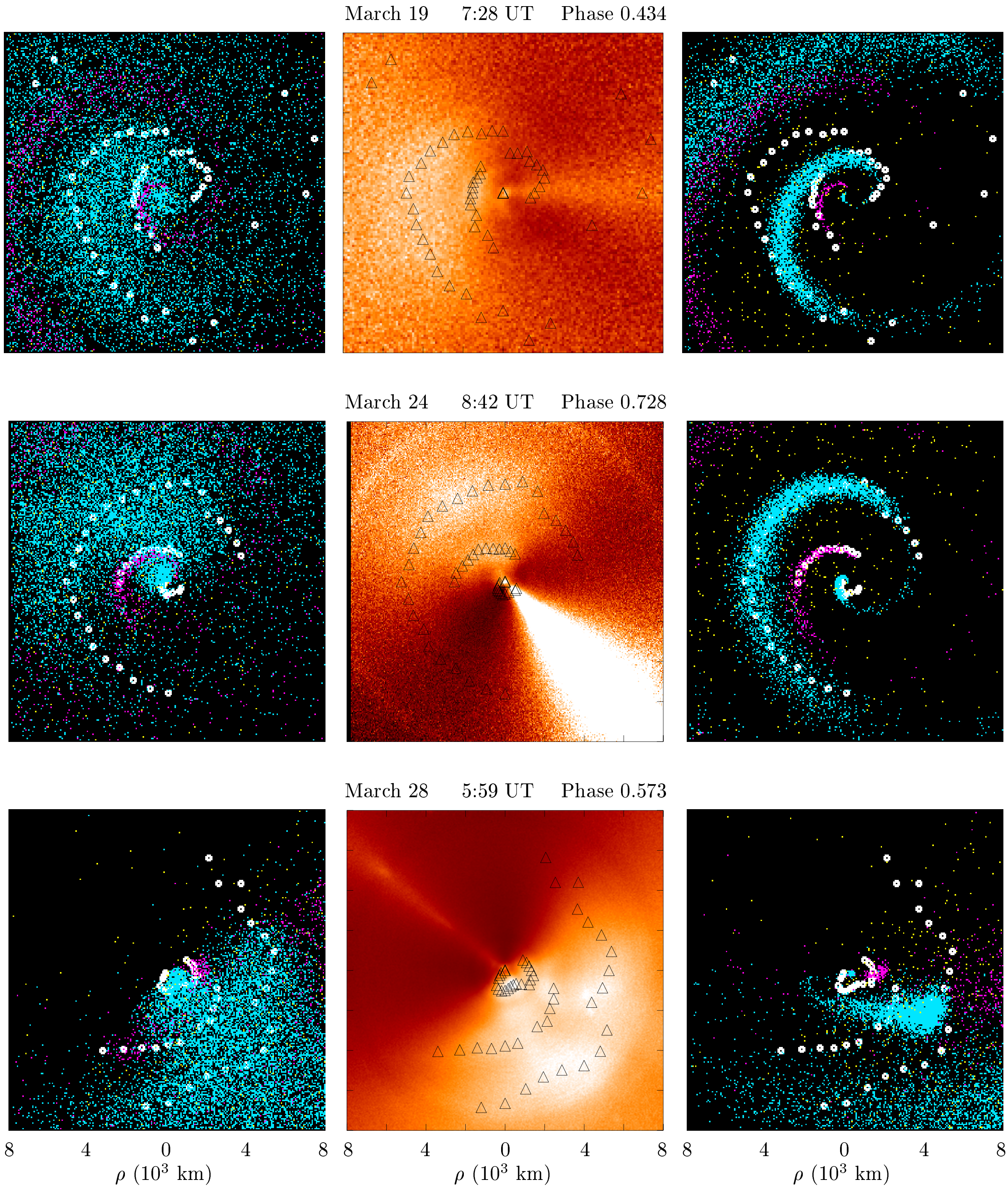

March 19 7:28 UT Phase 0.434
March 24 8:42 UT Phase 0.728
March 28 5:59 UT Phase 0.573
8
4
0
4
8
ρ (10³ km)

Figure 11

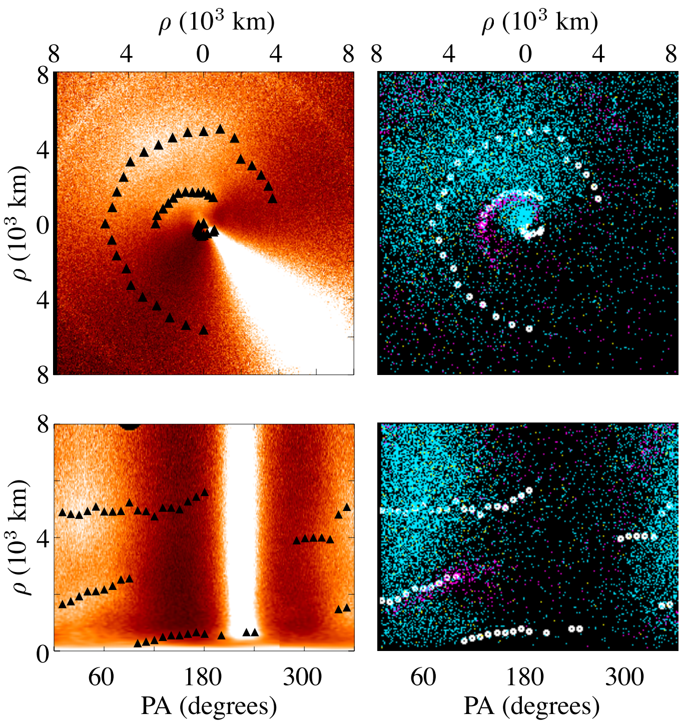

ρ (10³ km)
8
4
0
4
8
ρ (10³ km)
8
4
0
4
8
8
4
0
4
8
ρ (10³ km)
8
4
0
ρ (10³ km)
60
180
300
PA (degrees)
60
180
300
PA (degrees)

Figure 12

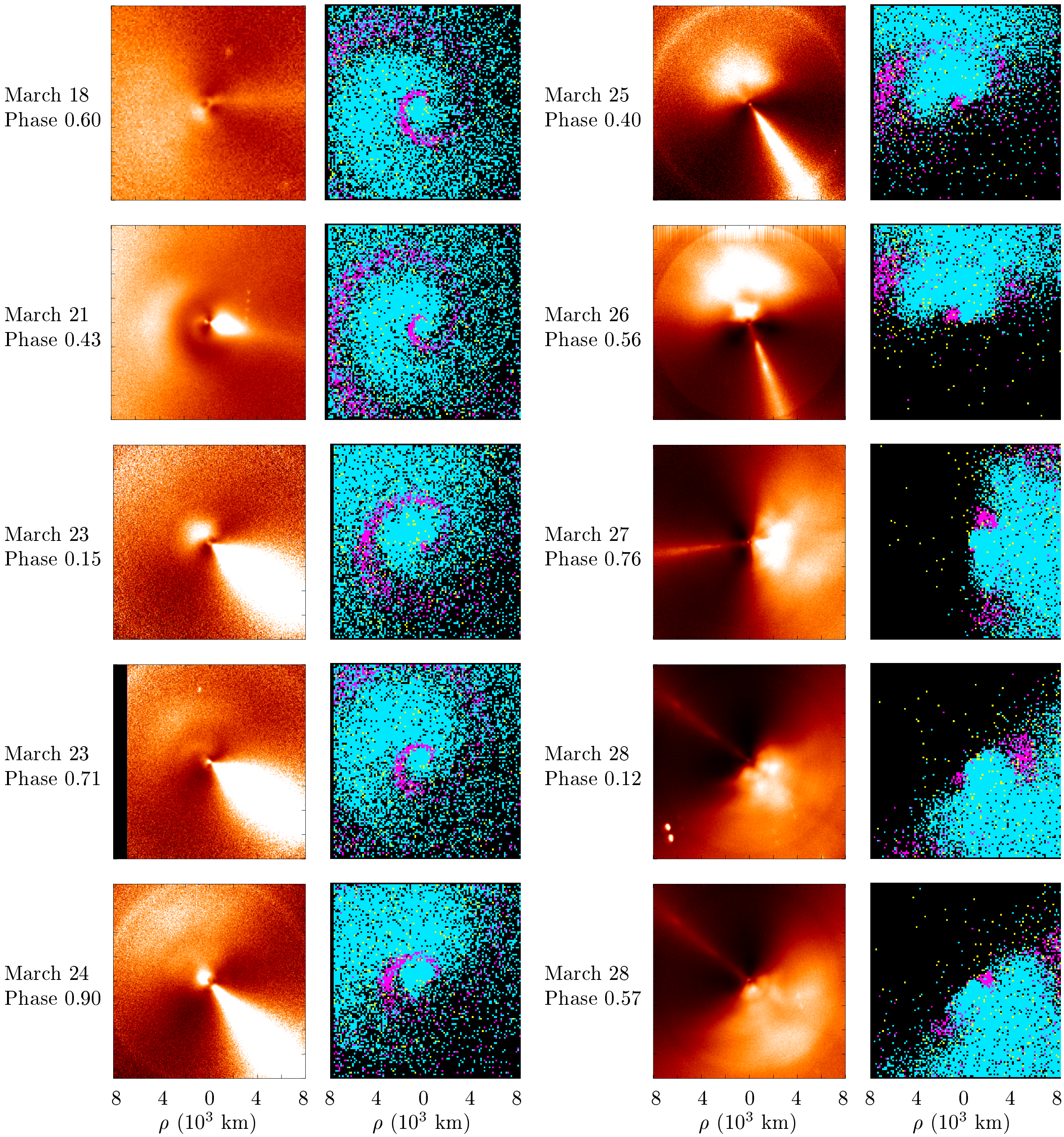
March 18
Phase 0.60
March 21
Phase 0.43
March 23
Phase 0.15
March 23
Phase 0.71
March 24
Phase 0.90
March 25
Phase 0.40
March 26
Phase 0.56
March 27
Phase 0.76
March 28
Phase 0.12
March 28
Phase 0.57
8 4 0 4 8
ρ (10^3 km)
8 4 0 4 8
ρ (10^3 km)
8 4 0 4 8
ρ (10^3 km)
8 4 0 4 8
ρ (10^3 km)

Figure 13

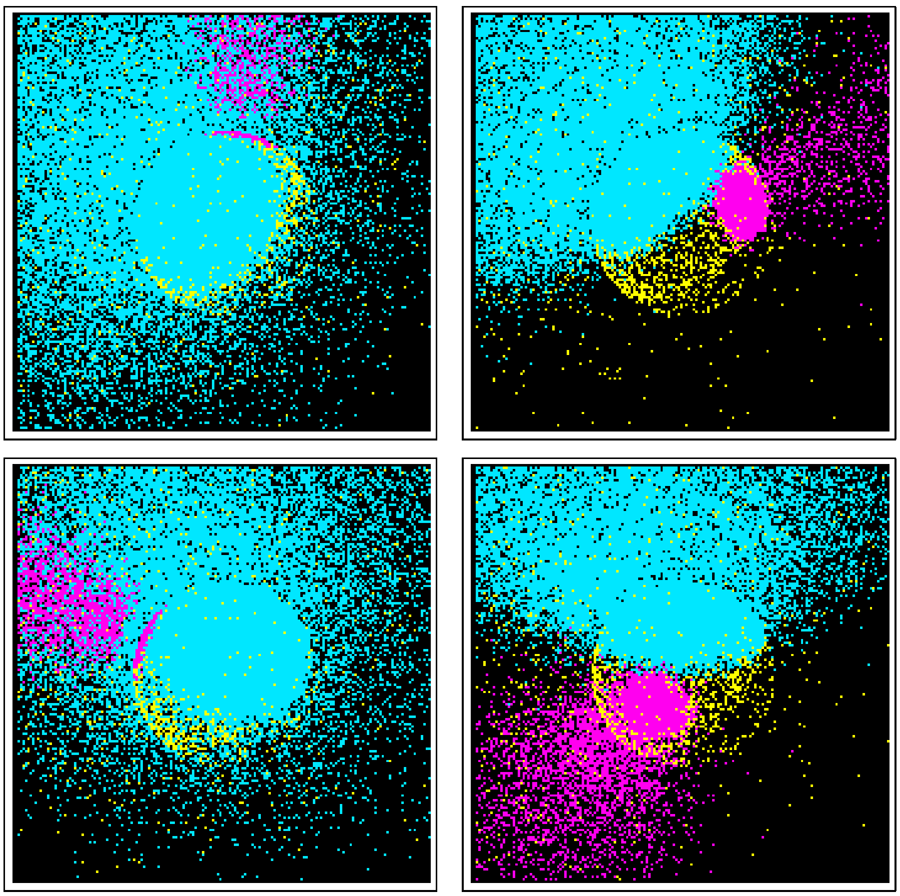

Figure 14

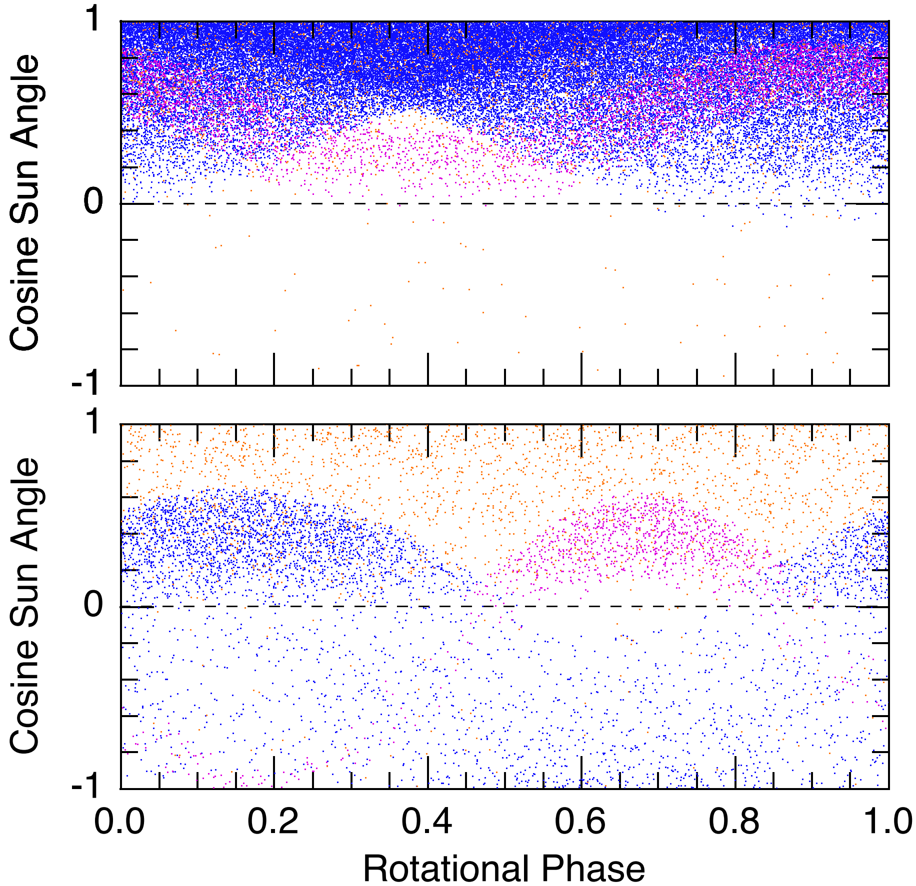
1
0
-1
Cosine Sun Angle
1
0
-1
Cosine Sun Angle
0.0
0.2
0.4
0.6
0.8
1.0
Rotational Phase

Figure 15

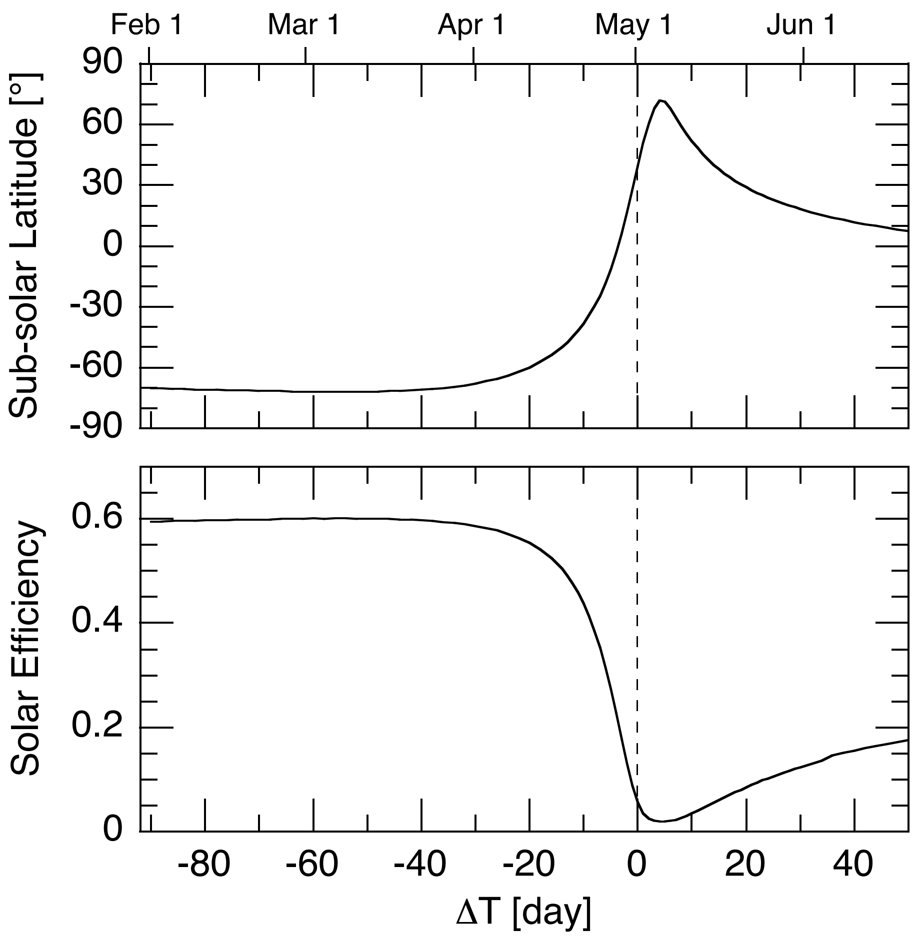
Feb 1
Mar 1
Apr 1
May 1
Jun 1
Sub-solar Latitude [°]
90
60
30
0
-30
-60
-90
Solar Efficiency
0.6
0.4
0.2
0
-80
-60
-40
-20
0
20
40
ΔT [day]

Figure 16

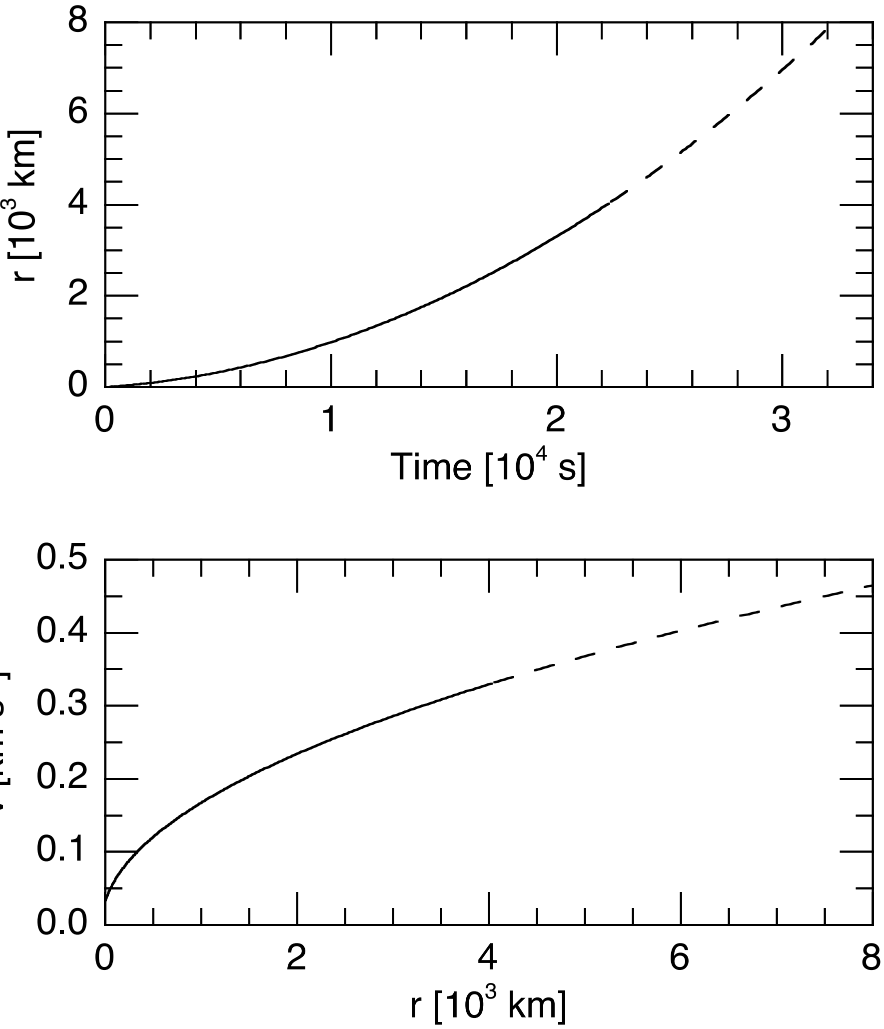

8
6
4
2
0
r [10³ km]
0
1
2
3
Time [10⁴ s]
0.5
0.4
0.3
0.2
0.1
0.0
v [km s⁻¹]
0
2
4
6
8
r [10³ km]

Figure 17

TABLE I

Observing Circumstances and Apparent Nucleus Orientation for Comet Hyakutake (1996 B2)

UT Date[a] (1996 March)	r_H (AU)	Δ (AU)	Interval (hr)	Phase Angle (°)	Sun PA (°)	Aspect Angle[b] (°)	Pole PA[b] (°)
18.31	1.185	0.253	0.1	37.1	97.7	161	286
19.30	1.166	0.223	0.5	36.8	94.0–93.9	162	277
20.36	1.144	0.192	3.9	36.6	88.8–87.9	162	263–261
21.39	1.123	0.165	0.9	36.9	81.0–80.7	160	244
22.35	1.103	0.141	0.2	38.3	70.7–70.5	156	227
23.36	1.082	0.120	7.8	41.5–43.3	58.7–53.2	149–146	214–210
24.35	1.062	0.106	8.2	48.6–52.1	41.5–34.8	137–132	203–200
25.33	1.041	0.102	9.9	59.3–64.7	23.6–16.4	122–115	195–192
26.36	1.019	0.108	2.3	74.8–76.1	5.2–3.9	101–100	183–180
27.32	0.999	0.122	3.2	85.3–86.6	331.4–207.3	88–86	80–62
28.19	0.980	0.140	4.2	92.6-93.9	196.2–197.1	79–77	35–33

[a] Mid-time.

[b] Apparent pole orientation of the nucleus as seen from Earth for our best model solution. Aspect angle is defined as 0° when the "north" pole points at Earth, while the pole PA is the position angle of the "north" pole.

TABLE II

Outburst Fragment Characteristics

Fragment ID[a]		T_0 [b] (1996 March)		a [c] (10^{-5} m s^{-2})	$\rho\, r$ [d] (10^3 kg m^{-2})
A	[1]	20.79	(20.5–21.0)	5.4±0.6	~1.4
B	[2]	21.96	(21.9–22.1)	5.4±0.2	~1.4
C		20.07	(19.6–20.5)	1.8±0.2	~4.2
D	[3]	21.54	(20.8–21.9)	2.2±0.4	~3.4
E		—		—	—
F	[6]	22.45	(20.1–23.3)	0.8±0.4	~9.4

[a] Fragments A–F in decreasing distance from the nucleus on March 25; values in brackets correspond to fragment IDs of Desvoivres et al. (2000).

[b] Separation date; viable range in parentheses is based on the uncertainty in a.

[c] Non-gravitational acceleration.

[d] The quantity $\rho\, r$ is the product of the fragment's density and radius.

TABLE III

Model Nucleus Solution

Model Parameter	Parameter Value[a]
Nucleus	
Pole Obliquity	108°
Pole Orbital Longitude	228°
Pole RA	205°
Pole Declination	–1°
Sidereal Period	0.2618 day
Primary Source Region	
Latitude	–66°
Longitude	202°
Radius	56°
Secondary Source Region	
Latitude	–28°
Longitude	10°
Radius	16°

[a] Estimated uncertainties are ±3° for the pole orientation and the source latitudes and radii, ±5° for source longitudes, and ±0.0001 day for the sidereal period.